




Revealing influence of warm bending on creep performance of heat-resistant 2.25Cr-1Mo-0.25 V steel

You Li¹, Song Huang^{2,*} , Hu Hui², Yile Han², Jiayi Huang¹, and Zhiping Chen^{1,*}

¹Institute of Process Equipment, Zhejiang University, 38 Zheda Road, Hangzhou 310027, Zhejiang, People's Republic of China

²School of Mechanical and Power Engineering, East China University of Science and Technology, Shanghai 200237, People's Republic of China

Received: 21 November 2022

Accepted: 28 January 2023

Published online:

11 February 2023

© The Author(s), under exclusive licence to Springer Science+Business Media, LLC, part of Springer Nature 2023

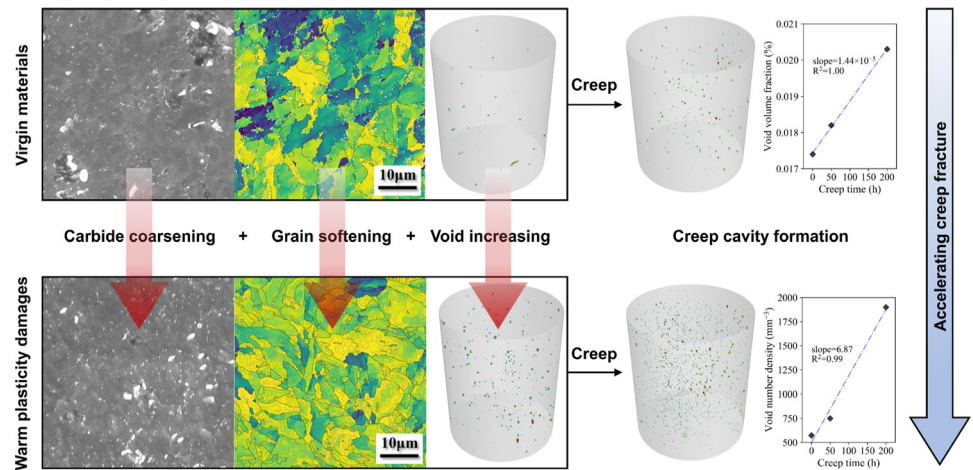
ABSTRACT

2.25Cr-1Mo-0.25 V steel has been widely used to manufacture hydro-processing equipment operating under harsh environments for its good creep performance. Warm bending, a common fabricating process of 2.25Cr-1Mo-0.25 V steel ring shells, inevitably changes the creep property of 2.25Cr-1Mo-0.25 V steel, but its detailed effect still remains obscure. In this work, we experimentally investigated the impact of warm bending on the microstructure and creep behavior of 2.25Cr-1Mo-0.25 V steel. First, a series of creep rupture tests were carried out at 482 °C and 350 MPa, in which test materials were extracted from an actually fabricated ring shell and its raw plate. Thereafter, the microstructures of test materials were semi-quantitatively analyzed by various characterization techniques, such as electron backscatter diffraction (EBSD) and three-dimensional high-resolution X-ray computed tomography (3D μ -XCT). Finally, warm forming induced microstructural degradation as well as their implication for creep was discussed in detail. Creep rupture tests showed that warm bending leads to a significant decrease in creep lifetime at the surface region of virgin plate but a slight decline at the central region of virgin plate. An inhomogeneous creep resistance distribution was thereby revealed along the thickness direction of the ring shell, which could not be completely eliminated by subsequent tempering at 705 °C for 8 h. Moreover, microstructural observations demonstrated that warm deformation leads to multiple microstructural deterioration, including carbide coarsening, ferrite matrix softening, void defect increasing, etc. Their combined action appears to accelerate the creep fracture behavior of 2.25Cr-1Mo-0.25 V steel. This work will contribute to the long-term safety and integrity assessment of 2.25Cr-1Mo-0.25 V steel structures.

Handling Editor: Naiquin Zhao.

Address correspondence to E-mail: huangsong@ecust.edu.cn; zhiping@zju.edu.cn

GRAPHICAL ABSTRACT



Introduction

High-temperature hydrogen-bearing pressure vessel serves as critical equipment in modern process industry (e.g., petroleum refinery industry, coal chemical industry, nuclear power industry, etc.) [1, 2]. In the past, 2.25Cr-1Mo was widely used to construct heavy-wall plate-bending ring shells for long-term high-temperature hydrogen service [3, 4]. However, the increasing desire of industrial scale, production efficiency and environmental requirement led to higher design parameters of process equipment. The components made from 2.25Cr-1Mo steel are ultra-thick, material consuming and uneconomical, resulting in a number of fabrication and maintenance challenges, thus cannot satisfy the advanced industry demands. Nowadays, the vanadium modified Cr–Mo low-alloy heat-resistant steel (2.25Cr-1Mo-0.25 V) has replaced 2.25Cr-1Mo steel serving as the material of choice for high-temperature high-pressure hydrogen-bearing equipment, mainly due to its superior high-temperature strength and better resistance to hydrogen attack [5, 6].

Since 2.25Cr-1Mo-0.25 V steel ring shell has to operate under harsh conditions (especially elevated temperature and high pressure) for a long time, creep damage needs to be considered in the equipment design and reliability analysis [1, 4, 7]. As we all

know, manufacturing inevitably changes material properties; hence, the creep performance of ring shell is expected to be very different from virgin plate. Fig. S1 depicts the fabrication procedure of heavy-wall plate-bending 2.25Cr-1Mo-0.25 V steel ring shell. Virgin plate (VP) is firstly heated to 650 °C, then bended into a ring shell in several minutes, followed by multi-layer submerged-arc welding and finally tempered at 705 °C for 8 h. For finished ring shell (FRS), the weld is generally regarded as a weak link, so its effect on the creep resistance of 2.25Cr-1Mo-0.25 V steel has attracted extensive attention from researchers. Song and his co-workers [8, 9] carried out a series of creep rupture tests on 2.25Cr-1Mo-0.25 V steel plate and its weld after tempering. Their results indicated a superior creep resistance of weld metal (WM) than base metal (BM) under 550 °C and 275–375 MPa. Elsewhere, using the digital image correlation (DIC) technique, Chu et al. [10] studied the heterogeneous creep behavior of 2.25Cr-1Mo-0.25 V steel plate welded joints under 455 °C and 400/420 MPa. According to their findings, the heat-affected zone (HAZ) has the highest steady-state creep rate, followed by BM, while WM shows the lowest steady-state creep rate. More related literature can be found in [11, 12]. In addition to welding, 2.25Cr-1Mo-0.25 V steel also encounters non-negligible deterioration during warm bending. Li et al. [13, 14] reported that warm bending induces a great

strength decline of 2.25Cr-1Mo-0.25 V steel plate. Wang et al. [15] found that 660 °C plastic deformation increases the hydrogen embrittlement susceptibility of 2.25Cr-1Mo-0.25 V steel plate. However, at present, there is a paucity of studies concerning how warm bending affects the creep performance of 2.25Cr-1Mo-0.25 V steel plate. Thus, a better understanding of the damage mechanisms of warm bending and its implications for creep failure of 2.25Cr-1Mo-0.25 V steel is required to improve the accuracy of structure integrity assessment.

So far, a lot of research has been conducted on how various damage modes (e.g., loading mode, service environment, manufacturing process, etc.) affect the creep behavior of heat-resistant steels. Zhang et al. [16] investigated the effect of creep-fatigue interaction damages on creep properties of P92 steel and found that the creep resistance of P92 steel is significantly degraded by creep-fatigue loading. Král et al. [17] studied the impact of pre-deformation on creep strength of 9%Cr steel and pointed out that severe plastic deformation could greatly soften this material. Chaudhuri et al. [18] revealed that thermal aging and pre-strain degrade the creep properties of 2.25Cr-1Mo steel, where carbide coarsening is proved to be the dominant mechanism. Hosseini et al. [19] systematically evaluated the influence of prior tensile and compressive deformation on subsequent creep response of 10%Cr steel and found that tensile pre-loaded specimens exhibit higher creep rate compared to compressive ones. Rui et al. [20] investigated a retired CrMoV bainitic gas turbine rotor and found the long-term service exposure could increase the creep strength of CrMoV steel but decrease the creep ductility. More related literature can be found in [21–23].

It is a common lore that the creep performance degradation of heat-resistant steels has its roots in the microscopic damages and defects. Recently, electron backscatter diffraction (EBSD) and three-dimensional high-resolution X-ray computed tomography (3D μ -XCT) have been extensively used in damage evaluation and failure analysis across a range of materials. For instance, Rui et al. [24] employed EBSD to quantify the creep damage of grains in austenitic stainless steel; Wang et al. [25] used EBSD to characterize the creep-fatigue damage in GH4169 superalloy; Guo et al. [26] applied high frame rate 3D μ -XCT to SA508 class 3 reactor pressure vessel steel to clarify the different behaviors between voids induced

by large and small inclusions under tensile deformation; Wang et al. [27] utilized 3D μ -XCT quasi in situ measurement to investigate the hydrogen-assisted void damage behaviors in 7075 Al alloy during plastic deformation. More related literature can be found in [25, 28–35]. However, to the extent of our knowledge, the two powerful characterization approaches are still scarcely applied to 2.25Cr-1Mo-0.25 V steel. Thus, EBSD and 3D μ -XCT should be adopted to characterize the microscopic defects caused by warm bending, which might provide better avenues for understanding damage mechanisms of 2.25Cr-1Mo-0.25 V steel.

In this work, a comprehensive investigation was conducted to clarify the impact of warm deformation on the creep resistance and microstructure of 2.25Cr-1Mo-0.25 V steel. Our test materials were extracted from an actually manufactured 2.25Cr-1Mo-0.25 V steel ring shell and its virgin plate. At first, a series of uniaxial creep rupture tests were carried out under 482 °C and 350 MPa. The difference in creep deformation and rupture behaviors between VP and FRS was analyzed. Moreover, the inhomogeneous creep performance along the thickness direction of FRS was also revealed and discussed. Secondly, warm bending induced microstructural degradation was carefully characterized by SEM, EDS, EBSD and 3D μ -XCT. The functional deterioration characteristics, including carbide coarsening, grain softening, intragranular lattice distortion and micro-void proliferation, were identified and discussed. Finally, a possible degradation mechanism of warm bending was proposed based on obtained experimental observations.

Materials and methods

Material preparation

Figure 1 illustrates a full procedure of material preparation. Test materials were cut from an actually manufactured 2.25Cr-1Mo-0.25 V steel ring shell and its raw plate provided by Lanzhou Lanshi Heavy Equipment Co., Ltd. Details are given in Table 1. For conciseness, we hereafter refer to the test ring shell as FRS and the test plate as VP. The circumferential direction, radial direction and axial direction of FRS correspond to the rolling direction (RD), normal direction (ND) and transverse direction (TD) of VP,

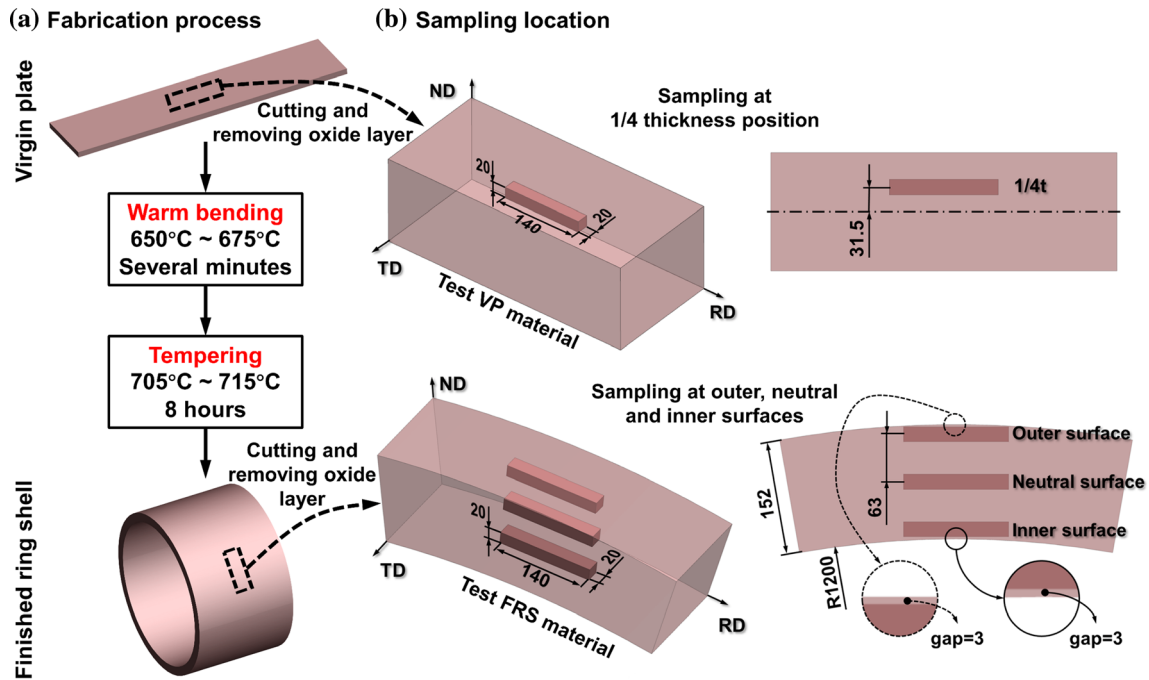


Figure 1 Preparation procedure of test materials: **a** manufacturing process of test ring shell, **b** sampling positions of test materials (unit: mm).

Table 1 Specifications of test materials

Test ring shell	
Raw material (i.e., virgin plate)	SA542 Type D Cl. 4 (930 °C normalized + 720 °C tempered)
Chemical composition (wt%)	C Cr Mo V Ni Mn Si P S Fe
	0.12 2.40 0.99 0.32 0.11 0.55 0.05 0.002 0.001 Bal
Forming operation	Warm bending at 650–675 °C
Post weld heat treatment	705 °C × 8 h
Inner diameter (mm)	2400
Thickness (mm)	152
Length (mm)	1700
Usage status	Brand new

respectively. To avoid confusion, RD, ND and TD are utilized to describe the material coordinate of both VP and FRS. Since the influence of welding was not thematized in this work, the welding heat-affected zone of FRS was excluded. That is to say, the investigated FRS materials here encountered only warm bending and tempering. The specific sampling positions are given in Fig. 1b. In the supplementary part, the mechanical strength and microstructure of surface region, 1/4 thickness position (1/4t) and center region of virgin plate were provided. As can be found, VP displays homogeneous mechanical and microstructural property distributions along its thickness direction (i.e., ND). Thus, we used the materials at 1/4t to represent VP materials. As for

FRS, the materials at outer, neutral and inner surfaces were all sampled for following experiments.

Creep rupture tests

Creep rupture tests were carried out at 482 °C and constant load corresponding to initial stress levels of 350 MPa. The creep testing operations were in accordance with Chinese standard GB/T 2039-2012 [36]. According to Nelson Curve in API RP 941 [37], the temperature limit of 2.25Cr-1Mo-0.25 V steel decreases with the increase in hydrogen partial pressure. When the hydrogen partial pressure exceeds ~ 13 MPa, the temperature limit of 2.25Cr-1Mo-0.25 V steel decreases to 510 °C and remains

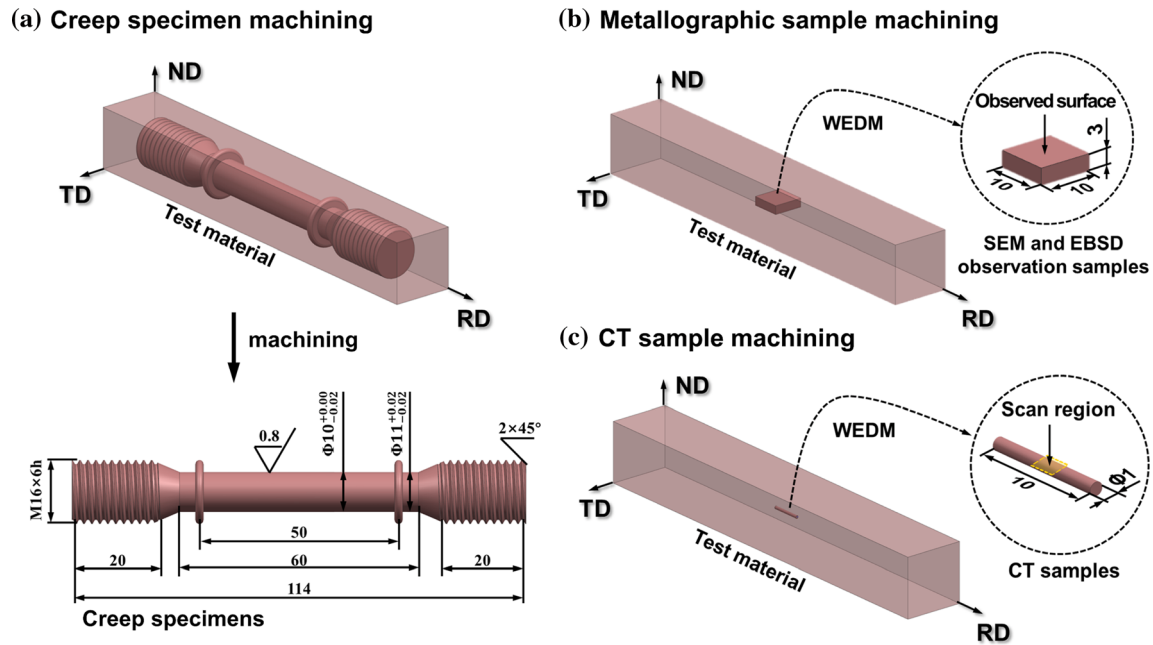


Figure 2 Machining procedure of **a** creep specimens, **b** metallographic samples and **c** CT samples (unit: mm).

unchanged. But the maximum design temperature of 2.25Cr-1Mo-0.25 V steel is limited to 482 °C by ASME BPVC-VIII-2 Code [38]. More details can be found in API Technical Report 934-B [39]. Nowadays, more and more hydro-processing equipment is designed with 482 °C [6], but their actual working temperature is much lower (mainly around 450 °C). Although, considering the test cost, we selected 482 °C as test temperature. To shorten the test time, a high stress level was also chosen. The dimensions of creep specimens are depicted in Fig. 2a. Notably, creep stress was controlled by a constant load applied by Changchun Qianbang QBR-100 high-temperature creep testing machine. Although some increase in stress will occur during the accelerated creep stage, constant load creep tests are still widely used [8–12].

Microstructure characterization

Metallographic samples ($10 \times 10 \times 3 \text{ mm}^3$) were cut from test materials without creep using a wire electric discharge machine (WEDM), as shown in Fig. 2b. The observed sections were gradually ground with 60–2000 SiC papers, polished with 1 μm diamond paste and cleaned with acetone. Thereafter, some of metallographic samples were etched with 4% nitric alcohol solution and observed by SEM (ZEISS GeminiSEM 500), while the others were vibro-polished

and used for EBSD measurements (Oxford Symmetry S3).

X-ray computed tomography (3D $\mu\text{-XCT}$)

For the purpose of cavity damage analysis, X-ray tomography based on phase contrast with high spatial resolution was adopted. The measurements were conducted by the device of Phoenix Nanotom M (General Electric, America) equipped with a high-resolution detector (3072×2400 pixels). To optimize the X-ray transmittance, needle-shaped samples ($\Phi 1 \times 10 \text{ mm}^3$) were cut from test materials without creep by WEDM, as shown in Fig. 2c. Constrained by the size of the detector, higher spatial resolution means a greater geometric magnification and thus a smaller field of view. Since spatial resolution is more important for cavity identification, a $188 \times$ microscope objective with a field of view of approximately $1.8 \times 1.4 \text{ mm}^2$ was used. That is to say, $\mu\text{-XCT}$ scans focused on the center regions of these needle-shaped samples ($\Phi 1 \times 1.4 \text{ mm}^3$, see the yellow rectangle in Fig. 2c). The $\mu\text{-XCT}$ scan parameters were optimized by trial and error. Specifically, scanning was performed at 80 kV tube voltage and 145 μA tube current; 1250 projections were collected with an exposure time of 1.67 s; low-energy X-rays were filtered with a 1 mm aluminum filter. For each sample, the acquired tomographic dataset ($\sim 11 \text{ GB}$)

comprised 1250 X-ray transmission projections, and the tomographic reconstruction was performed based on a filtered back-projection algorithm provided by the phoenix datosix CT software. The voxel size of reconstructed 3D volumes was $700 \times 700 \times 700 \text{ nm}^3$.

Cavity segmentation and characteristic analysis

Cavity defect analysis was implemented using VG Studio MAX 3.4 software. For a better comparison, a unified region of interest (ROI) with a size of $\Phi 0.8 \times 1 \text{ mm}^3$ was extracted from the reconstructed 3D image set of each μ -XCT sample, as depicted in Fig. 3. Generally, cavity defects have much lower X-ray mass attenuation coefficients than solid phases, so darker features in the ROI can be recognized as voids. Indeed, when reading the gray value distribution of ROI, one could find dual peaks: the first peak with lower gray values captures the void defects, and the second peak with higher gray values denotes the solid phases. As a consequence, grayscale thresholding was employed here for cavity segmentation, and the specific threshold value of each ROI was determined by the intersection of the two humps. Figure 4 gives a typical example of grayscale threshold selection for clarity. As can be seen, thin solid lines here accurately outline the boundary of cavity, indicating an acceptable accuracy of segmentation. It should be noted that small cavity like a single voxel can be affected by noise in the CT data [40]. Hence, the smallest distinguishable 3D defect that can be resolved with confidence is generally taken as about 3 times the pixel size [41]. Accordingly, only cavities larger than 27 voxels were included in detailed quantitative analyses.

The above segmentation provided the binary images of solid phases and void defects for further

analysis. In order to quantify the void characteristics, some representative parameters (i.e., number density, volume fraction, equivalent sphere diameter, circumscribed sphere diameter, sphericity, elongation and flatness) were statistically analyzed based on the defect data from the μ -XCT tests. Their definitions and calculations could be found in many literatures [42, 43].

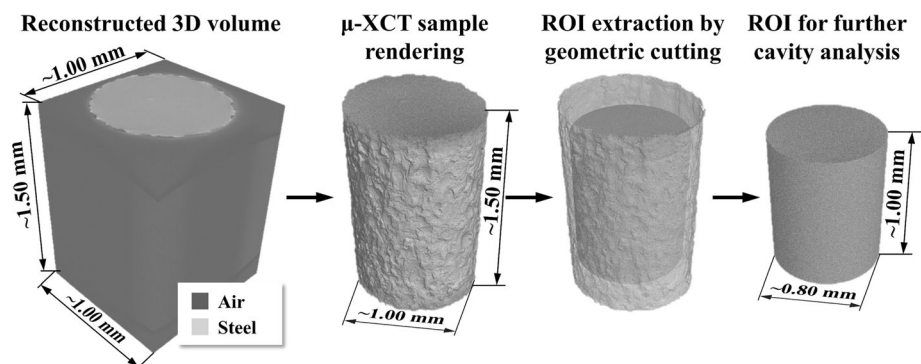
Results

Creep deformation and rupture behaviors

Figure 5 shows the creep strain curves of VP and FRS materials, and their average steady-state creep rates are listed in Table 2. As can be seen, FRS specimens exhibit a significant performance degradation compared to VP specimens. Specifically, the creep lifetime of VP specimens is about 1100 h, while that of FRS specimens decreases by 19–76% (ranging from 264 to 908 h). Moreover, the steady-state creep rate of FRS specimens (ranging from $1.02 \times 10^{-8} \text{ s}^{-1}$ to $3.88 \times 10^{-8} \text{ s}^{-1}$) is much higher than that of VP specimens (c.a. $0.57 \times 10^{-8} \text{ s}^{-1}$). The secondary stage creep of VP specimens reaches 800 h occupying more than 70% of their creep life, while the secondary stage creep of FRS specimens is no longer than 400 h which occupies less than 50% of their creep life. From the above results, we speculate that warm bending triggers significant degradation on 2.25Cr-1Mo-0.25 V steel which cannot be fully recovered by current tempering.

In addition, Fig. 5 and Table 2 also suggest an inhomogeneous distribution of creep resistance in FRS along the thickness direction. In our creep rupture tests, the neutral surface materials (average creep life = 899 h) have the longest creep life,

Figure 3 Extraction strategy of a unified ROI for cavity analysis.



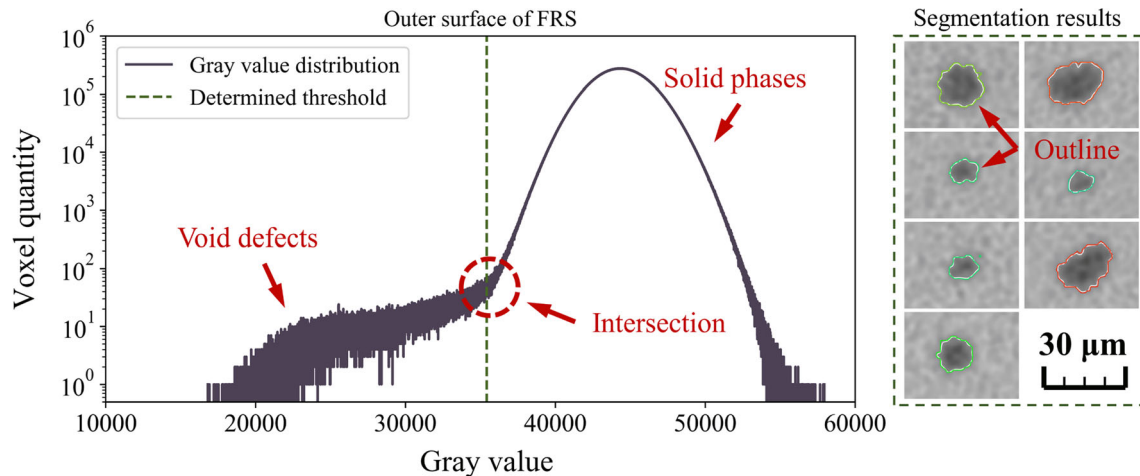


Figure 4 Determination of grayscale threshold value for cavity segmentation in the outer surface of FRS.

Figure 5 Creep strain curves of VP and FRS materials.

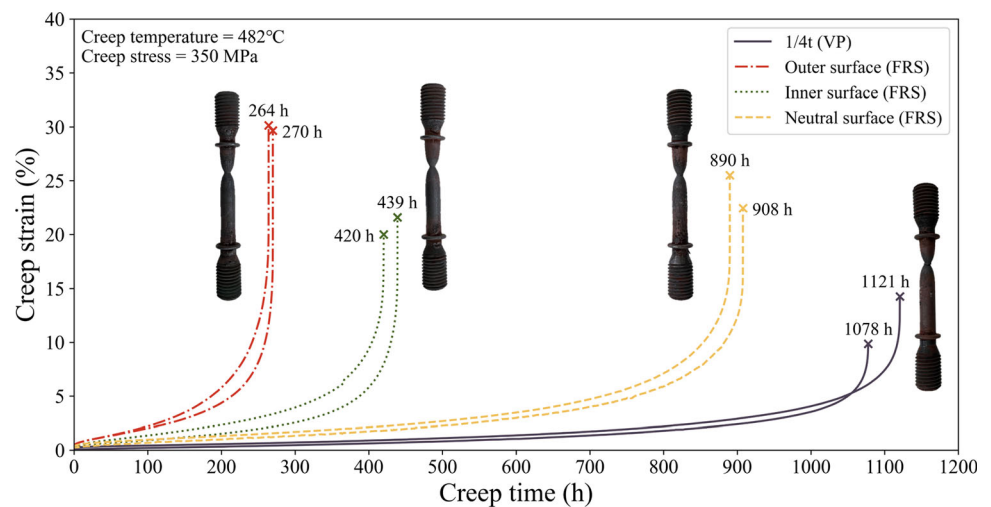


Table 2 Average steady-state creep rate of VP and FRS materials

Sampling position	Average steady-state creep rate (10^{-8} s^{-1})
1/4t (VP)	0.57
Outer surface (FRS)	3.88
Neutral surface (FRS)	1.02
Inner surface (FRS)	1.91

followed by the inner surface materials (average creep life = 430 h), while the outer surface materials (average creep life = 267 h) exhibit the worst creep property. Regarding the steady-state creep rate, center materials are also superior than surface materials. For instance, the average steady-state creep rate of outer surface materials is 4 times as high as that of neutral surface materials. The decreased behavior of creep life at different thickness positions of FRS

implies three distinct damage states induced by warm bending: tension deformation damage, compression deformation damage and tension–compression transition damage. In this work, the greatest reduction in creep life is caused by the tension deformation, followed by compression deformation, while the tension–compression transition damage has little influence.

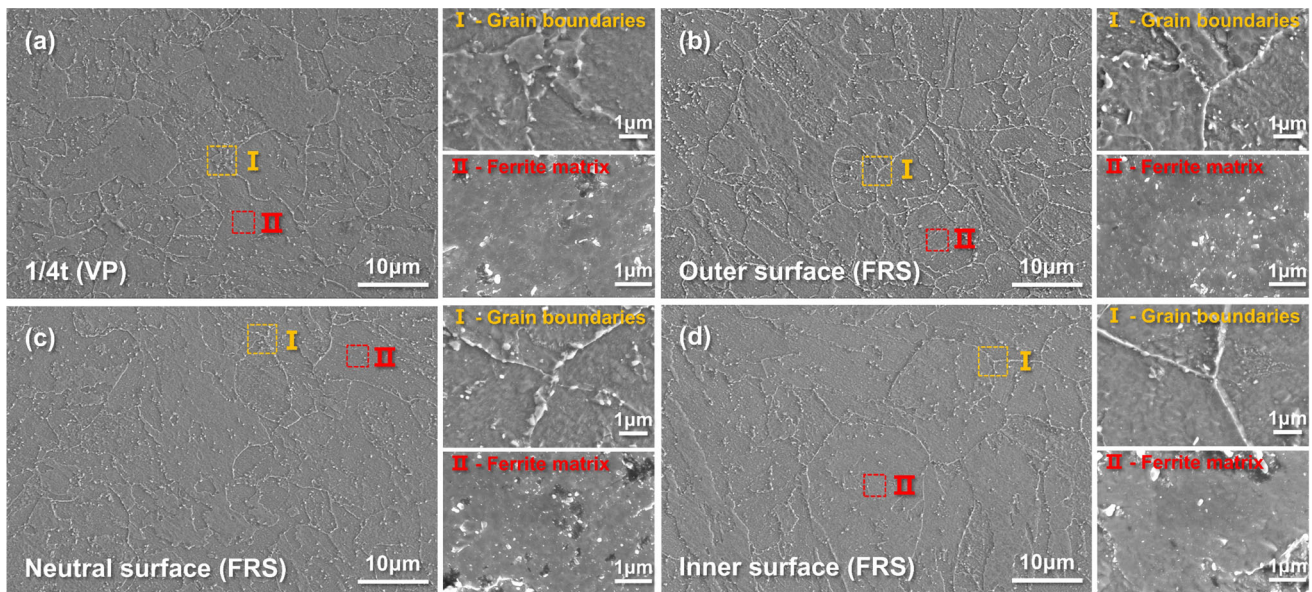


Figure 6 SEM images of VP and FRS materials before creep: **a** 1/4t of VP, **b** outer surface of FRS, **c** neutral surface of FRS and **d** inner surface of FRS.

Microstructure characteristics by SEM, EDS and EBSD

Figure 6 shows SEM images of VP and FRS materials. Here, the gray matrix is ferrite (FM), the island-shaped uplift is a complex phase of martensite and retained austenite (M-A island), the slightly uplifted stripes are the grain boundaries of prior austenite (PAGBs), and the white particles are dispersed carbides (such as MC and $M_{23}C_6$). Overall, the carbide quantity of FRS materials is slightly higher than that of VP material. Furthermore, the carbides at PAGBs and FM were characterized at higher magnifications (see the insets referred by Regions I and II in Fig. 6). As can be seen, most carbides in VP material are dispersed in the matrix without obvious grain boundary segregation, whereas some quantities of carbides (c.a. 150 nm) can be observed uniformly distributed along grain boundaries in FRS materials. Also, there are more clusters of large-size precipitates (c.a. 100 nm) in the FM of FRS materials than VP material.

For quantitative analysis, Fig. 7 gives the statistical results of carbides in Fig. 6. The carbide identification was carried out by Image-Pro Plus 6.0 software which is widely used for quantitative analysis of grains, precipitates or voids [14, 15, 44]. Here, the precipitates below 4 pixels were considered noise and not included in the statistics. Many studies [45, 46]

reported, when carbides grow above 60 nm, their pinning effect on dislocations will be greatly reduced. Therefore, the carbides here were pre-divided into two categories (i.e., small size and large size), and 60 nm equivalent circle diameter (D_{equ}) was used as critical value. As can be seen, there are more small-size carbides in VP material than in FRS materials, while the situation is reversed for large-size carbides. This suggests, a part of fine carbides in VP material grow and coarsen during warm bending and subsequent tempering. In FRS, central and surface regions exhibit a similar size distribution of carbides.

In these SEM images (see the insets of Region II in Fig. 6), the point-like carbides (c.a. 10–60 nm) are thought to be vanadium-rich carbides (MC) which were also observed by Takeda Hiroyuki [47] in 2.25Cr-1Mo steel and evidenced to be prolongedly stable under high temperatures. The large carbides with irregular round, oval or rhomboidal shapes are likely to be chromium-rich precipitates (M_7C_3 or $M_{23}C_6$), which are relatively prone to coarsening under the drive of temperature [48]. EDS analysis was carried out on a cluster of ~ 150 nm precipitates in the outer surface of FRS. The result (see Fig. 8) corroborates, these large-size precipitates are enriched in chromium, which gives indirect proof that they are M_7C_3 or $M_{23}C_6$. The good creep resistance of 2.25Cr-1Mo-0.25 V steel is mainly attributed to the stable dispersion of fine MC carbides [45] and is also

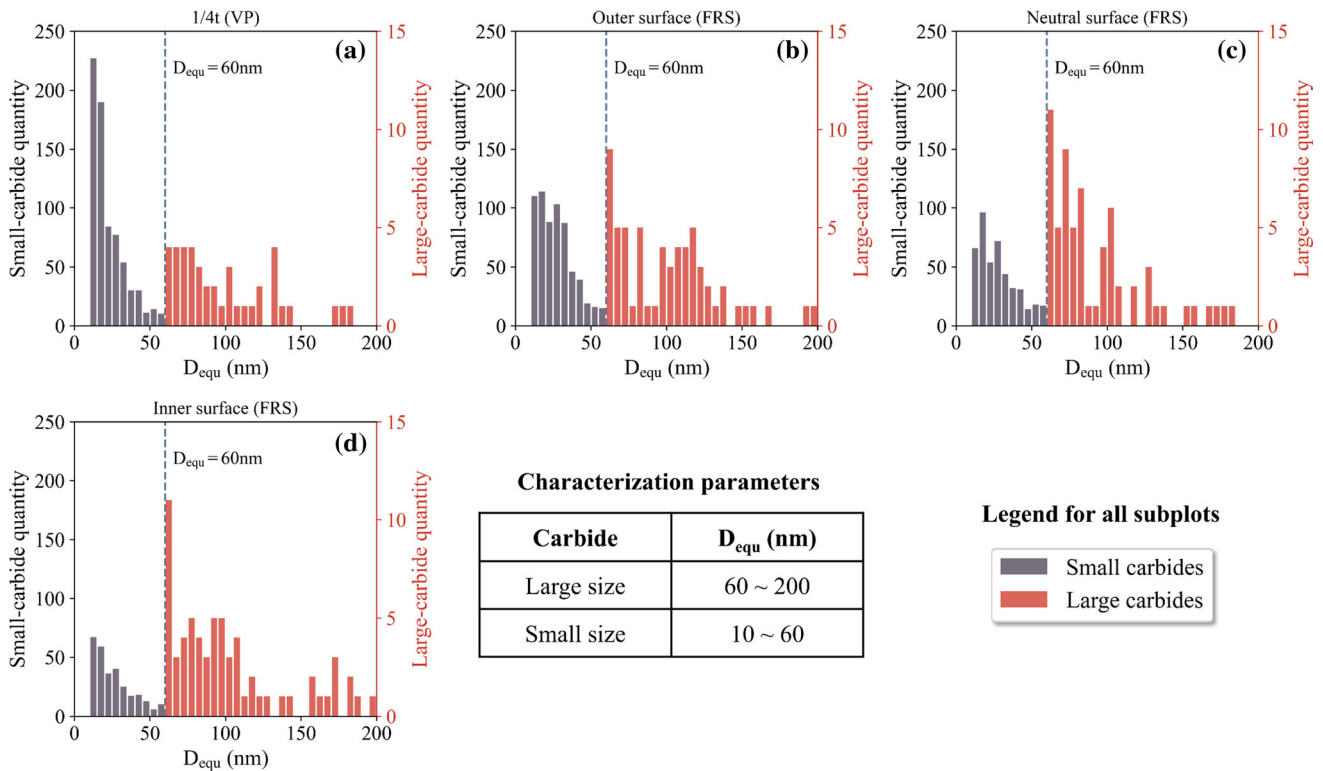


Figure 7 Carbide statistics of VP and FRS materials before creep (calculated based on Fig. 6): **a** 1/4t of VP, **b** outer surface of FRS, **c** neutral surface of FRS and **d** inner surface of FRS.

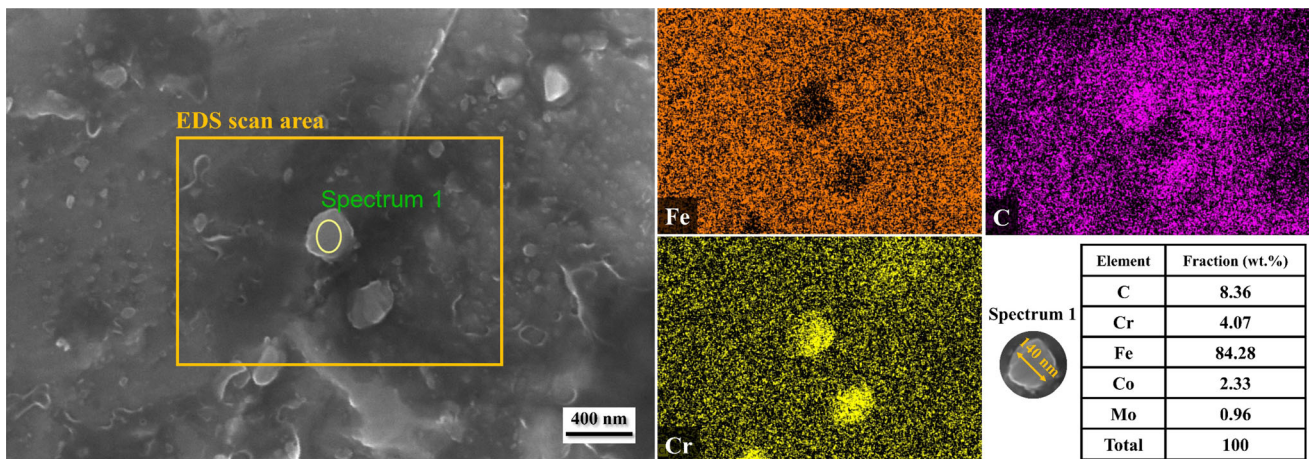


Figure 8 EDS analysis of a ~ 140 nm carbide cluster in the FM of FRS.

due to in matrix solid solution alloying elements (Cr, Mo, V, Ti and Ni, etc.) [49]. The former acts as strong obstacles for dislocation motion, while the latter improves the matrix plastic resistance. The growth and coarsening of M_7C_3 or $M_{23}C_6$ were widely investigated in the thermal or thermo-mechanical process of 2.25Cr-1Mo-0.25 V steel (such as hot

forming [50], normalizing [51] and tempering [52]). Although the carbide evolution of 2.25Cr-1Mo-0.25 V steel during warm bending and subsequent tempering is not well understood, it can be deduced that the conversion of MC to M_7C_3 or $M_{23}C_6$ and their coarsening simultaneously occur during this period. Thereby, the deleterious effects on solution

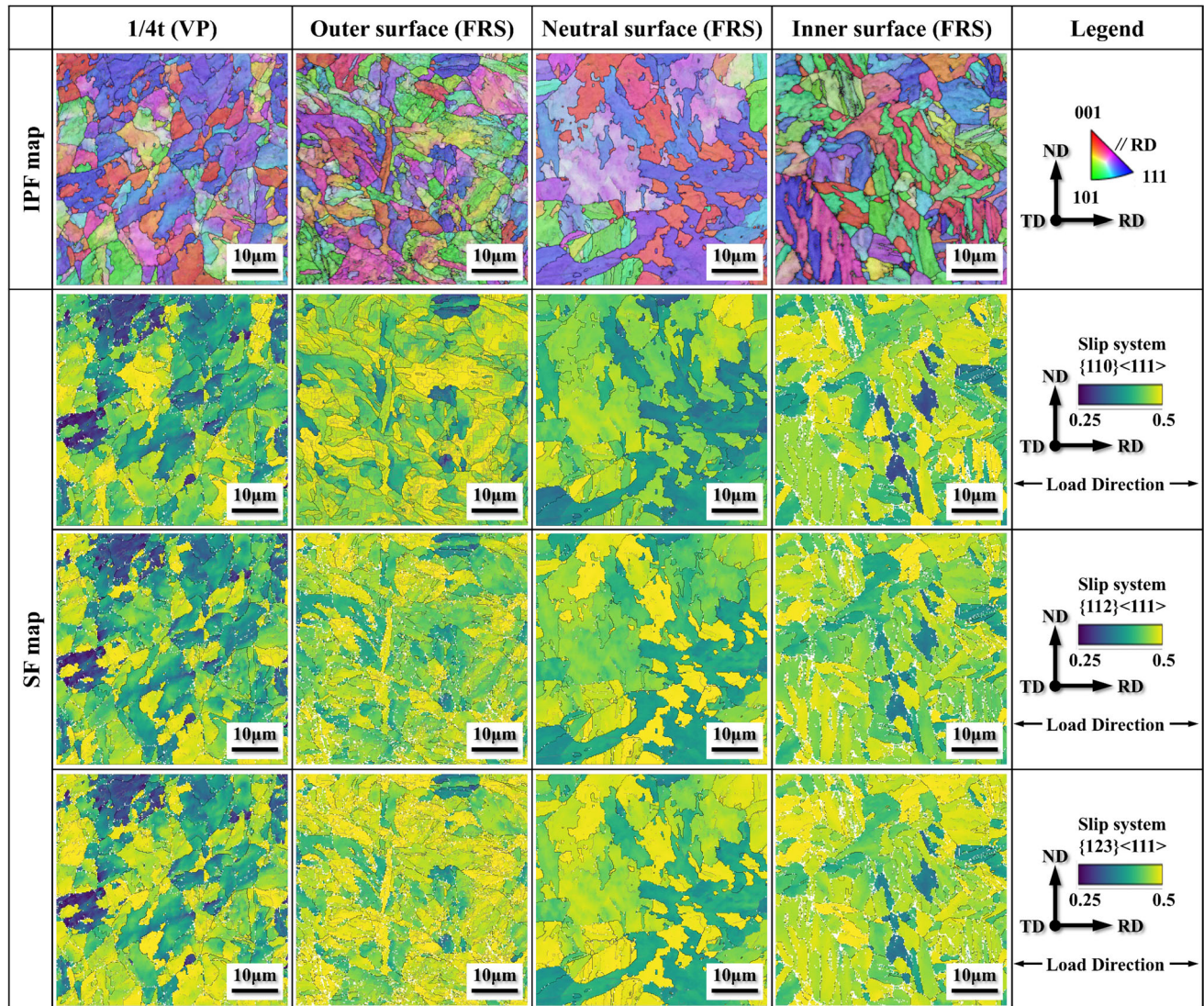


Figure 9 EBSD maps of VP and FRS materials before creep (step size = 0.2 µm, raster = 250 × 250, scan region 1).

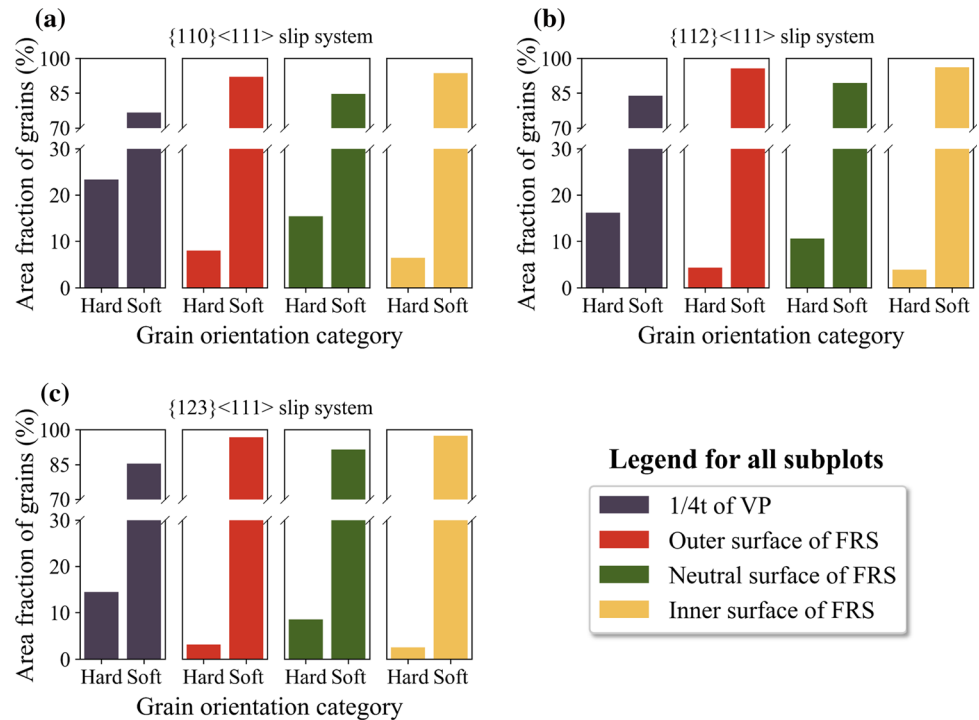
strengthening and dispersion strengthening caused by carbide behaviors may preliminary explain the great loss of creep life of FRS compared to VP.

Figure 9 (up-side) shows the inverse pole figure (IPF) maps of VP and FRS materials. The black solid lines represent the high-angle grain boundaries ($\geq 15^\circ$, HAGBs), and the gray ones indicate the low-angle grain boundaries ($2^\circ\text{--}15^\circ$, LAGBs). As can be observed, the 1/4t materials of VP and the central materials of FRS are quite similar in grain morphology and orientation, and mainly exhibit HAGBs. As for surface regions of FRS, many LAGBs are observed, and the grains of outer and inner surface materials are circumferentially deformed, especially those marked in green. Specifically, the grains of

outer surface materials are elongated circumferentially, whereas the grains of inner surface materials are compressed circumferentially (also appearing as radially elongated). This corresponds to warm bending induced inhomogeneous plastic deformation along the thickness direction of FRS. That is to say, in FRS, the central area is the low deformation zone for grains whereas the surface and near-surface regions are high deformation zones for grains. Moreover, recrystallization is not found here, implying the microstructure evolutions during warm bending and subsequent tempering are primarily ascribed to strain strengthening, dynamic recovery and static recovery. The limited capability of recovery mechanism on HAGBs may explain the phenomenon that warm

Figure 10 Area fraction of hard- and soft-oriented grains in VP and FRS materials before creep:

a $\{110\} \langle 111 \rangle$ slip system, **b** $\{112\} \langle 111 \rangle$ slip system and **c** $\{123\} \langle 111 \rangle$ slip system.



bending induced grain-scale degradation still remains in the FRS materials (especially in surface regions).

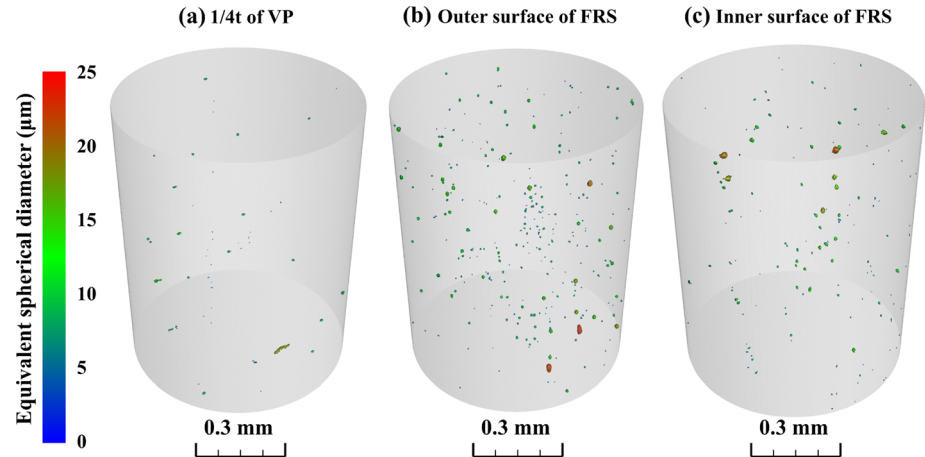
It is well acceptable that $\{110\} \langle 111 \rangle$ slip, $\{112\} \langle 111 \rangle$ slip and $\{123\} \langle 111 \rangle$ slip are the dominant deformation modes of body-centered cubic (BCC) single crystals. They also play a pivotal role in the plastic deformation behavior of BCC polycrystalline metals. Therefore, based on the obtained EBSD data, Schmid factor (SF) maps for $\{110\} \langle 111 \rangle$, $\{112\} \langle 111 \rangle$, $\{123\} \langle 111 \rangle$ slip systems of VP and FRS materials were calculated, as shown in Fig. 9 (down-side). The stress axis used for SF calculation is in line with the creep rupture test, that is, along RD of test materials (see horizontal direction in Fig. 9). And each pixel displays the maximum SF value of 12 (or 24) equivalent slip systems. A larger SF value refers to a softer crystallographic orientation, meaning a higher probability of activation of the corresponding slip system. Obviously, most of grains in VP material are biased toward hard orientation whereas the situation for FRS materials is the opposite. For FRS, soft-oriented grains dominate the surface regions, while the numbers of hard- and soft-oriented grains are essentially comparable in the central region. Moreover, Fig. 10 depicts the area fraction of hard- and soft-oriented grains in VP and FRS materials. Here, the SF of 0.4 was utilized as the cut-off value [53], and

to make our analysis more convincing, the EBSD data of another $50 \times 50 \mu\text{m}^2$ scan areas (see in the supplementary materials) were also involved. Apparently, for all of three slip systems, the hard-oriented grains show a higher area fraction in VP material than in FRS materials. As for FRS materials, the center has the higher area proportion of hard-oriented grains than the outer and inner surfaces. In surface regions of FRS, soft-oriented grains occupy almost 95% of the area. Based on the above analysis, one could speculate that VP material is more resistant to creep deformation than FRS materials. And in the FRS, the creep resistance of center material is thought to be higher than that of surface materials, which differs from the conventional wisdom that thick-walled structures have the weakest center. This could also well explain the different steady-state creep rates of VP and FRS materials (see Table 2).

Cavity characteristics by 3D μ -XCT

Figure 11 displays the 3D visualization of micro-void segmentation in VP and FRS materials before creep, and the void population is colored according to their equivalent spherical diameter. Obviously, there are few micro-voids in the VP material, while the surface regions of FRS exhibit much more cavities, which could be ascribed to the fabrication damage.

Figure 11 μ -XCT volume rendering of voids in VP and FRS materials before creep: **a** 1/4t of VP, **b** outer surface of FRS and **c** inner surface of FRS.



Specifically, the highest number density of void is found for the outer surface of FRS (573 mm^{-3}), followed by inner surface of FRS (300 mm^{-3}), and the VP material shows the lowest number density of void (107 mm^{-3}). Analogously, the void volume fraction maximizes at 0.0174% for the outer surface of FRS, the inner surface of FRS is the second (0.0113%), and VP material has the lowest void volume fraction (0.0022%). It can be found that the number density and volume fraction of voids in the FRS's outer surface material are almost 5 and 8 times higher than those in the VP material, respectively. In contrast, the creep rupture time of the former is less than a quarter of that of the latter (see “Creep deformation and rupture behaviors” Section), which is likely linked with the cavity proliferation during warm bending. As discussed in “Creep deformation and rupture behaviors” Section, no recrystallized grains have been observed in all test materials; thus for FRS materials, these forming induced micro-voids are considered to be incurable by $705 \text{ }^\circ\text{C} \times 8 \text{ h}$ tempering. That is to say, warm bending will generate a large number of micro-defects in 2.25Cr-1Mo-0.25 V steel, leading to a remarkable creep resistance deterioration of ring shell.

Figure 12 shows the size distributions and morphology characteristics of voids in VP and FRS materials without creep. From Fig. 12a and b, it can be found that the equivalent and circumscribed sphere diameters of void population in all test materials exhibit similar distributions and can be well described by normal fitting. The equivalent sphere diameter of voids mainly ranges from 3 to 10 μm in VP material, while that of FRS materials is concentrated in 3–15 μm . Compared to VP, the increase in

3–10 μm and 10–15 μm voids in FRS suggests the nucleation and growth of cavities during warm bending, respectively. Although compressive deformation is generally considered to have an inhibitory effect on defects, statistical analysis shows that there are still more micro-voids in the inner surface of FRS than in VP, which may be attributed to the stress triaxiality induced by warm bending. Notably, for the inner surface of FRS, warm bending mainly increases the voids between 5 and 15 μm , but less voids below 5 μm are generated than the outer surface of FRS, suggesting that the cavity formation is somewhat depressed in the compression zone of FRS. Similar findings can be easily inferred from the void circumscribed sphere diameter distribution. As for the morphological parameters of voids, their distributions also conform to the normal law. Specifically, for the cavity population of VP and FRS, sphericity mainly distributes at interval of 0.5–0.7, elongation is concentrated in 1–2, and flatness ranges from 1 to 1.5. That is to say, before creep, the cavities in VP and FRS are mainly sub-globose and ellipsoidal, and the latter accounts for the majority. The average void sphericity values of FRS materials are a little higher than that in VP, and their distributions are slightly deflated toward the high values (see Fig. 12c). The average elongation and average flatness of voids in FRS both show a decline compared with VP, and a range contraction toward lower values is also discerned for them (see Fig. 12d and e). Considering a consensus that void nucleation tends to sprout into sphere, the different void morphologies between VP and FRS further corroborate void generation during warm bending.

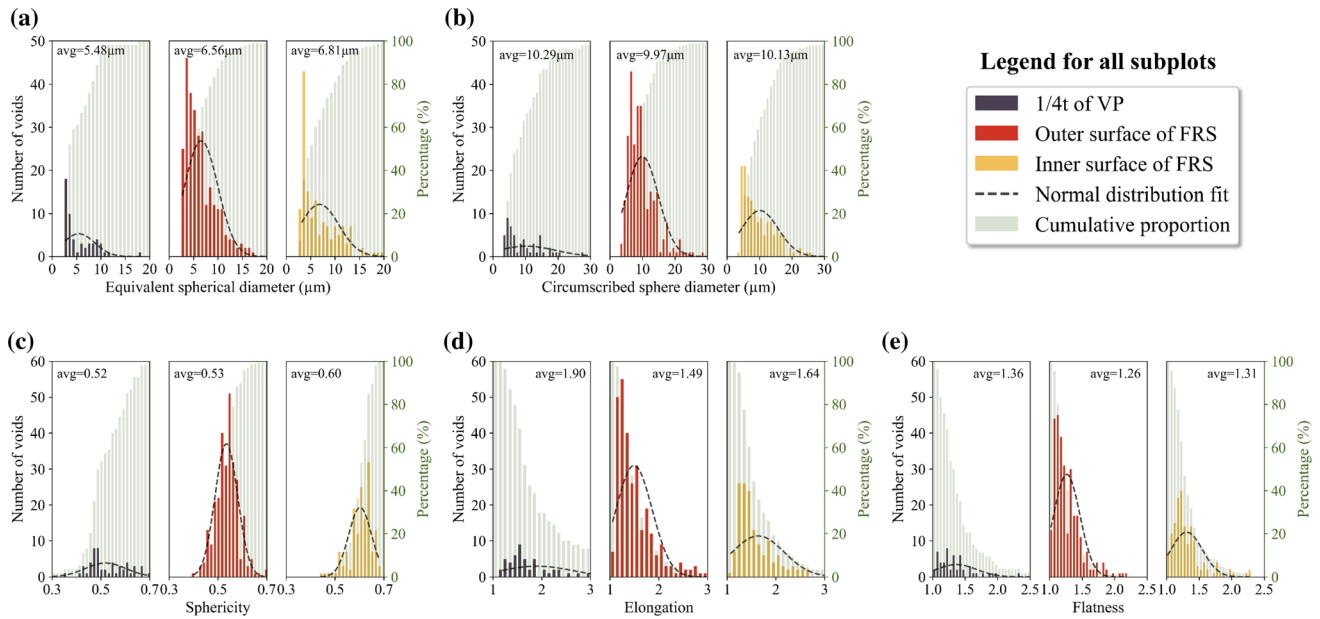


Figure 12 Void characteristics of VP and FRS materials before creep: **a** equivalent spherical diameter, **b** circumscribed sphere diameter, **c** sphericity, **d** elongation and **e** flatness.

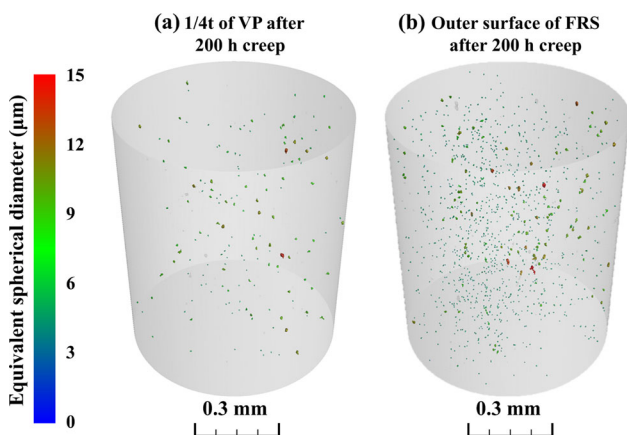


Figure 13 μ -XCT volume rendering of voids in VP and FRS materials after 200 h creep (the applied stress is along the vertical direction): **a** 1/4t of VP and **b** outer surface of FRS.

As is well known, micro-voids provide a particularly strong effect on the creep behavior of metals [54], and their behaviors (i.e., nucleation, growth and coalescence), thereby, have been widely investigated [55, 56]. Considering the cup-and-cone fracture of all creep rupture specimens, the ductile fracture mechanism dominated in our short-time creep tests. To date, numerous studies have demonstrated that there is a critical cavity volume fraction for the coalescence of voids which is the final stage in the ductile fracture of metals. In other words, the space between voids becomes smaller as the void volume fraction

increases; when the critical value is reached, the linking of voids can occur, leading to a rapid failure. Therefore, compared to VP, the increase in void density in FRS is speculated to accelerate the creep cavity evolution of 2.25Cr-1Mo-0.25 V steel. Strong evidence can be found in Figs. 13 and 14. The former displays the spatial distribution of voids in VP and FRS materials with 200 h creep, and the latter gives their detailed void characteristics. Apparently, after 200 h creep, the outer surface of FRS shows much more voids than VP. The number density of cavities at the outer surface of FRS (1900 mm^{-3}) is almost 7 times that of VP (275 mm^{-3}). Likewise, the volume fraction of cavities at the outer surface of FRS (0.0203%) is over 3 times that of VP (0.0062%). Moreover, the equivalent and circumscribed sphere diameters of voids in the outer surface of FRS primarily concentrated in the size interval of 4–6 μm and 5–10 μm , respectively, while VP shows a comparatively homogeneous void size distribution over a wider range. This suggests that the higher void number density of FRS is attributed to the increase in smaller voids and indicates a faster creep cavity proliferation in FRS. Moreover, the shape distribution of voids in VP and FRS materials supports above speculation as well. As can be found in Fig. 14c and d, despite 200 h creep, these parameters still conform to the normal distribution well. In contrast to VP, the

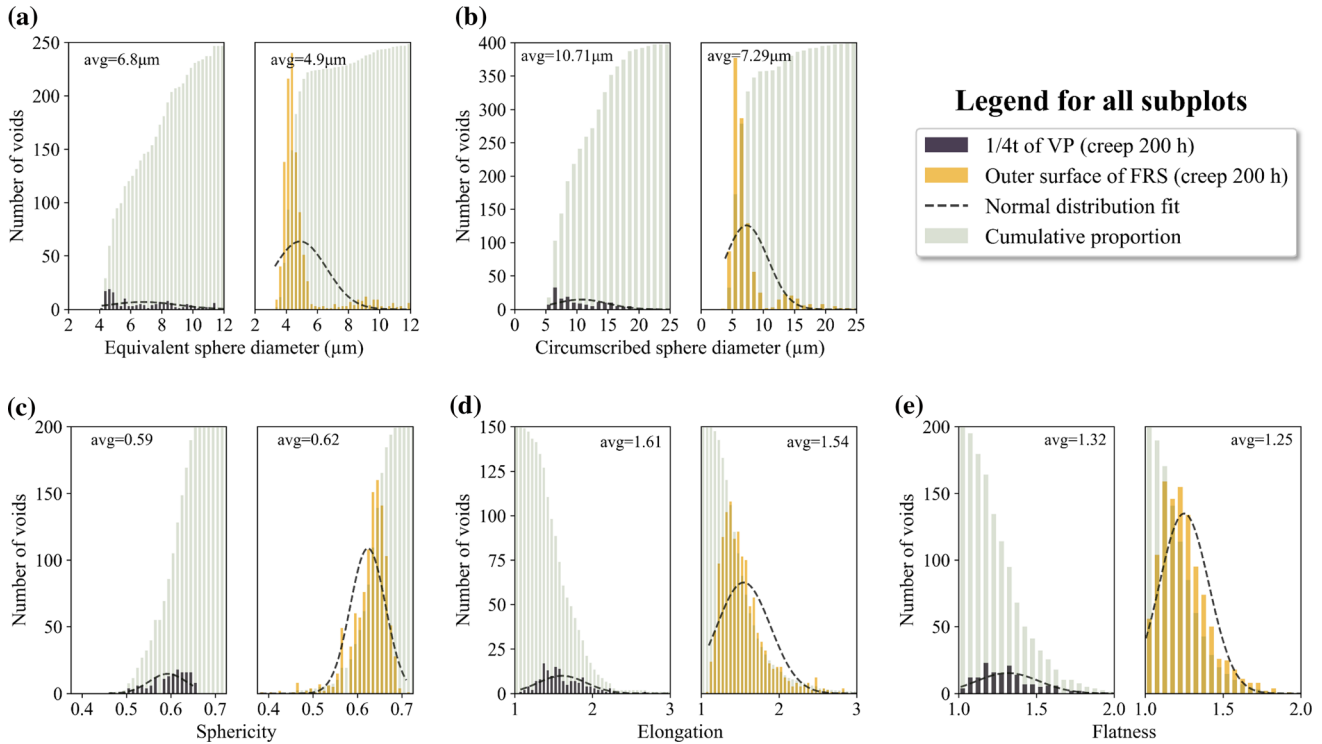


Figure 14 Void characteristics of VP and FRS materials after 200 h creep: **a** equivalent spherical diameter, **b** circumscribed sphere diameter, **c** sphericity, **d** elongation and **e** flatness.

outer surface of FRS exhibits a slightly higher average void sphericity, and its void sphericity distribution is expanded toward higher values (see Fig. 14c). As opposed, the elongation and flatness of voids in the outer surface of FRS show lower average values in comparison with VP, and their peaks in FRS are shifted toward lower values as well. This void geometry difference is observed to occur as an indirect result of the easier spherical creep cavity formation in FRS than in VP.

From another perspective, our μ -XCT results reveal creep cavity evolution in VP and FRS materials. Considering that the outer surface of FRS has the shortest creep rupture time among all tested materials, the following focuses on its creep cavity behaviors. For clarity and credibility, we reorganize the aforementioned relevant μ -XCT characterization results, and provide additional data of the outer surface of FRS with 50 h creep, as shown in Fig. 15. Apparently, in the creep time range from 0 to 200 h, a longer creep aging leads to a linear increase in the number density and volume fraction of void (see Fig. 15b). Taken macroscopic creep behavior into consideration, the primary creep regime is little and thus can be neglected, whereas the followed steady-

state creep regime lasts for ~ 200 h and occupies the majority of creep life (~ 267 h). Therefore, one can say that the creep cavity damage develops linearly in the steady-state creep regime. Note that, creep damage is well known to accelerate drastically in the tertiary creep regime, but is not involved here for its relatively shorter duration. In terms of void size, the average circumscribed sphere diameter decreases monotonically with the increasing creep time, which can be ascribed to the continuous formation of smaller voids with the circumscribed sphere diameter of 5–10 μm (see Fig. 15c). For the outer surface of FRS after 200 h creep, apart from the sharp peak, there is an additional hump at the circumscribed sphere diameter of ~ 15 μm (see red circles in Fig. 15c). Despite the small absolute amount, this weak hump still implies a non-negligible void growth behavior as well as its coexistence with dominant proliferation in the steady-state creep regime. Besides, no ultra-large cavities (over 50 μm here) or so-called micro-cracks are observed in our μ -XCT results, suggesting void coarsening has not occurred yet. In other words, void linking is not markedly activated in the secondary creep stage, which coincides with domain knowledge. When it

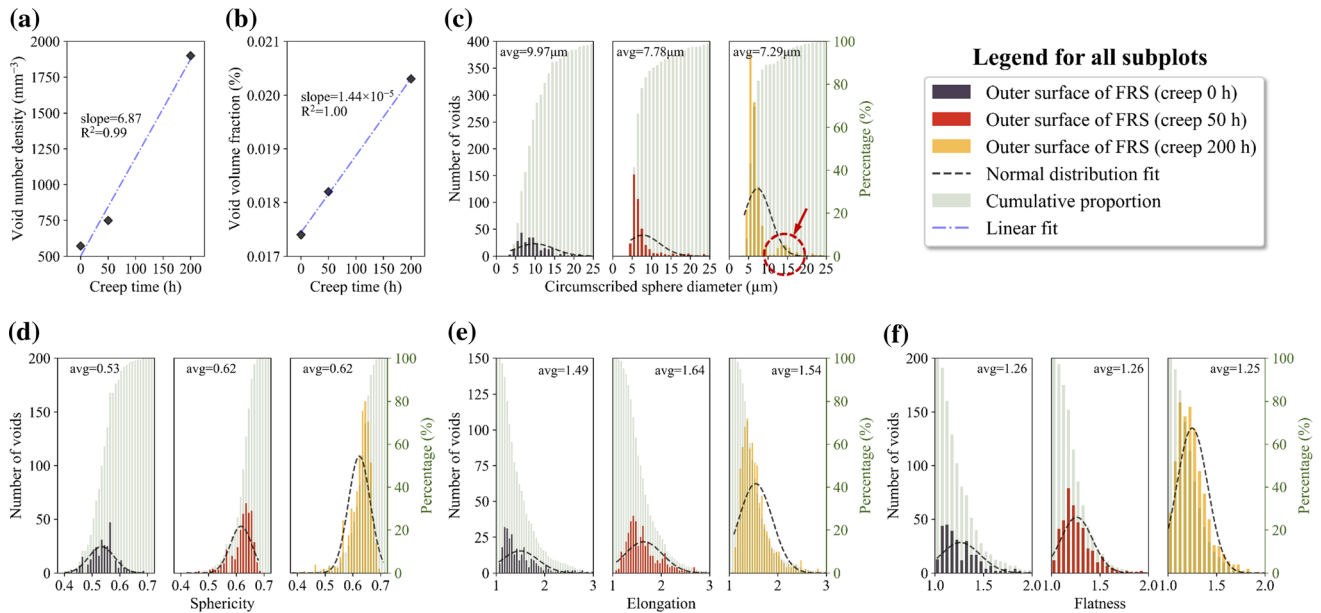


Figure 15 Creep cavity evolution in the outer surface of FRS: **a** number density, **b** volume fraction, **c** circumscribed sphere diameter, **d** sphericity, **e** elongation and **f** flatness.

comes to void shape, the selected shape parameters all behave differently (see Fig. 15d–f). The average void sphericity rises from 0.53 to 0.62 after initial 50 h creep and remains stable during followed creep aging (up to 200 h). As creep time increases, the void sphericity distribution continuously concentrates toward higher values. For 50 h and 200 h crept materials, almost 80% of the voids are close to either spherical or ellipsoidal, and situated in the sphericity range of 0.6–0.7. The average void elongation shows a trend of rising first and then falling with longer creep time (up to 200 h). The comparison of void elongation distributions after 0 h and 50 h creep reveals a slight decrease in voids with elongation less than 1.4, but a marked increase in voids with higher elongation, especially the ones with elongation over 2. On the one hand, this implies a change trend of void shape from quasi-sphere into prolate ellipsoid; on the other hand, for shorter creep times, void growth is more pronounced than void generation. In the subsequent creep damage process (that is, from 50 to 200 h), there is a dramatic increase in voids with elongation below 2, but no significant change is observed in voids with higher elongation. Hence, one can conjecture that void formation is more pronounced than void growth with the development of steady-state creep. Last but not least, the average void flatness is roughly constant for 0 h, 50 h and 200 h creep aged samples. Their void flatness

distributions are all concentrated in the range of 1–1.5, which means no broadly ellipsoidal cavities or flat micro-cracks are formed in the secondary creep regime. Many studies have reported that large creep cavities with complex shape occur in the secondary and tertiary stages of brittle creep, such as diffusion creep [57]. The absence of such voids may be attributed to the ductile fracture mechanism under 482 °C and 350 MPa creep loading on the one hand, and the limited cavitation capacity of decay and steady-state creep on the other hand.

Discussion

Qualitative analysis on microstructural degradation caused by warm bending

From the experimental analysis given above, the microstructural degradation caused by warm bending can be preliminary elucidated. The microstructure of 2.25Cr-1Mo-0.25 V steel has been widely investigated [8, 9, 13, 14]. Despite of some differences in these investigations, carbides are well agreed to play a fundamental role in the thermo-mechanical properties of 2.25Cr-1Mo-0.25 V steel. Based on our SEM observations in this work (see Fig. 6), the following carbide behaviors can be revealed. In VP, a large number of small-size carbides are dispersed in

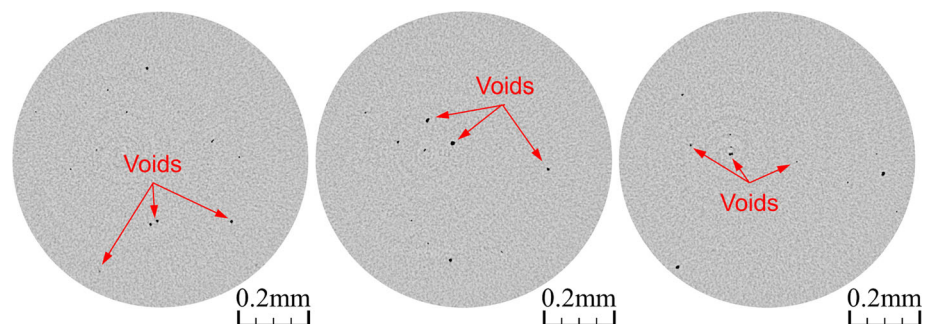
the ferritic matrix, some large-size carbides are clustered, and few carbides are segregated at grain boundaries. After warm bending and subsequent tempering, these carbides are overall coarsened, severely clustered and undesirably segregated. Similar carbide behaviors were also reported in the 660 °C forming process of 2.25Cr-1Mo-0.25 V steel plate by Wang [15] and 705 °C tempering process of 2.25Cr-1Mo-0.25 V steel casting by Jiang et al. [52]. Although the specific carbide evolution during the integrated process of warm bending and tempering has not been fully understood yet, Ostwald ripening of fine particles may explain these carbide behaviors. In detail, when the small-size carbide population reaches its equilibrium amount at a certain temperature, the coarsening of large-size carbides takes place at the expense of small-size ones [11]. Additionally, a strain-induced precipitation phenomenon was found in the hot deformation process (over 900 °C) of 2.25Cr-1Mo-0.25 V steel forging by Wang [50], but no significant difference in carbides between the surface and center materials of FRS is observed here. This can be attributed to the relatively low plastic deformation in the surface regions of 152 mm thick ring shell (below ~ 10%).

Apart from carbides, dislocation also has a critical impact on creep performance of 2.25Cr-1Mo-0.25 V steel plate. Since the normalizing and tempering treatments after hot rolling, the dislocation density in VP is relatively low. As reported in [15], the dislocation density of 2.25Cr-1Mo-0.25 V steel plate rises with larger 660 °C plastic deformation (up to 5%), owing to the competitive mechanism of strain hardening and dynamic recovery. In the strain hardening mechanism, dislocation generally proliferates, moves, interacts with carbides, tangles with each other, piles on at grain boundaries and so on, leading to numerous lattice defects. In the dynamic recovery mechanism, dislocation rearrangement and

annihilation take place to reduce lattice distortion. During warm bending, the surface regions of FRS have a comparatively high plastic deformation and thus strain hardening occupies a preponderant place, whereas the central region of FRS undergoes little plastic deformation and hence dynamic recovery dominates. Our EBSD results show, compared to VP, there is an apparent LAGB increase in the outer and inner surface regions of FRS but a marked LAGB decline in the central region of FRS. As we all know, LAGBs correlate with the degree of intragranular distortion, which indirectly reflects the dislocation density. For our test ring shell, the current tempering cannot completely cure the warm bending induced dislocation defects in the surface regions. It is well accepted for 2.25Cr-1Mo-0.25 V steel that the reduction of dislocation density during tempering is accompanied by material softening [14]. That is to say, the warm bending induced inhomogeneous dislocation density distribution can be alleviated via prolonger tempering treatment at the expense of strength loss.

Last but not least, warm bending also promotes the formation of micro-voids as probed by 3D μ -XCT. The void behaviors during plastic deformation of metal materials have been studied for more than 40 years [58]. As is well known, cavity initiation sites within the microstructure are generally associated with hard secondary phase particles [59]. The mismatch between deformation responses of ferrite matrix (soft phase) and precipitates (hard phase) is one of the most important causes of void nucleation in the warm bending process of 2.25Cr-1Mo-0.25 V steel. There are two typical ways for void nucleation: a debonding of the matrix/particle interface or particle cracking [60]. Here, we focus on the former as it is more common in carbides with $D_{\text{equ}} < 1 \mu\text{m}$. For submicron-scale carbides, void nucleation shows a strong dependency on carbide size [26]. The bonding

Figure 16 CT images of typical voids in FRS materials after 200 h creep.



energy of matrix/carbide interface decreases with increasing carbide size, so voids are prone to nucleate at larger carbides. Figure 16 presents some CT images of typical voids in FRS materials after 200 h creep. As for smaller carbides, warm bending induced dislocation pile-up can increase their near-field stress and thus facilitate the breaking of the matrix/carbide interface [60]. Taken together, both small- and large-size carbides in 2.25Cr-1Mo-0.25 V steel serve as nucleation sites, and the plastic strain generated by warm bending acts as the driving force for nucleation.

Possible correlation between creep resistance degradation and warm deformation

The creep rupture tests of VP and FRS materials reveal that warm bending leads to an inhomogeneous degradation in the creep resistance of large thickness 2.25Cr-1Mo-0.25 V steel plate along the normal direction which cannot be completely erased by subsequent 705 °C × 8 h tempering. This residual inhomogeneous deterioration effect should be traced back to the inhomogeneous microstructural degradation generated by warm bending. The degradation characteristics caused by warm bending have been carefully discussed in “Qualitative analysis on microstructural degradation caused by warm bending” Section, but it still remains unclear how warm deformation affects the creep behavior of 2.25Cr-1Mo-0.25 V steel at the microscopic scale. The exact mechanism could not be fully clarified yet since there are few related investigations on 2.25Cr-1Mo-0.25 V steel and our experimental observations here are still limited. Nevertheless, some possible underlying correlations are discussed below.

As viewed from the dislocation creep mechanism, the creep resistance of metals has largely linked to their resistance to thermally activated dislocation motion [61]. When it comes to 2.25Cr-1Mo-0.25 V steel, its good creep strength is mainly attributed to the effective pinning force of fine carbides that are stably dispersed in ferrite matrix over a long term, especially the vanadium-rich carbide MC [45]. Our SEM analysis confirms the growth and coarsening behaviors of nanoscale precipitates during warm bending. The larger precipitates are less stable than the smaller one and more likely to coarsen under creep exposure, as observed in many CrMoV steels

[49]. After a certain creep duration, the size of precipitates in FRS is thus rationally presumed to be larger than that in VP. The ability of carbides to stabilize dislocation structure decreases with their increased size [11]. Therefore, when a certain load is applied, the dislocations in FRS materials are thought to move more easily than these in VP material, which manifests as a higher creep strain rate of FRS materials compared to VP material. Moreover, the growth and coarsening of precipitates also consume a huge amount of solid solution alloying elements in the ferrite matrix (such as Cr, Mo, V, Ti and Ni) [62], making the bainite grains easier to deform. At the same creep aging time, greater loss of solid solution elements, namely softer grain matrix, is expected for FRS materials since their carbides may coarsen more severely than those in VP. This presumption may further explain the discrepancy in minimal creep rate between VP and FRS materials.

From another point of view, the creep rupture behavior of metals can also be regarded as a ductile failure process in which cavity evolution plays an important role. As previously discussed, the different plastic behavior between soft and hard phases is an important reason for void nucleation. Our EBSD analysis finds that warm bending rotates some of the bainite grains to softer orientations in which sliding systems are more easily activated. Considering the heterogeneous plastic strain of various microstructures under creep load [63], these softer grains are more likely to suffer plastic strain during prolonged operation. Consequently, a more severe deformation mismatch of ferrite matrix and intragranular carbides is expected in these soft-oriented grains. In other words, micro-voids prefer to generate within soft-oriented grains over hard-oriented ones. Based on this, under a certain creep exposure, the surface regions of FRS that has the largest number of soft-oriented grains should suffer most creep cavities, followed by the central region of FRS, while VP material is the last. Although direct evidence is not observed in this work, our μ -XCT results in Fig. 13 provide important corroboration to the above conjecture. In addition, FRS exhibits higher initial void number density as well as initial void volume fraction than VP, which is considered to accelerate the development of creep cavity population. Specifically, initial voids, especially larger ones, exacerbate the strain localization in their vicinity, which helps them continue to expand on the one hand [64] and

promotes the formation of creep cavities on the other hand [26]. Furthermore, the higher initial void density, that is, a smaller inter-void spacing, can advance the moment of void linking [65] and thus shorten the duration of creep failure.

In summary, a synergistic effect of multiple microstructural deterioration induced by warm deformation, including coarsened carbides, decreased matrix hardness, intensified carbide/matrix deformation mismatch and increased cavity defects, could preliminary explain the discrepancy in creep behavior between VP and FRS as well as the inhomogeneous creep performance in FRS. Notwithstanding, it has to be emphasized that our above arguments have not been evidenced here, and further exploration is needed. Additionally, the creep behavior and microstructural damages of 2.25Cr-1Mo-0.25 V steel at lower temperature and lower load were not investigated in this work. Therefore, readers should interpret our findings cautiously based on this limitation.

Creep life prediction based on machine learning (ML)

In the past century, a large number of models have been proposed to predict the creep behavior of various metals [66], including time–temperature parameter (TTP) method (e.g., Larson-Miller [67], Manson-Haferd [68], Manson-Succop [69], etc.), damage parameter method based on continuum creep damage mechanics (CDM) model [70], phenomenology-based prediction method based on creep curve (e.g., θ -projection method [71], Ω -method [72], etc.) and so on. In engineering practice, despite of limited extrapolation precision, Larson-Miller equation is most widely used to convert creep life from high temperature to low temperature or from high stress to low stress because of its simplicity.

However, due to the complex mechanism of warm bending damages, we cannot directly apply these traditional models to accurately quantify the creep performance of warm-bended 2.25Cr-1Mo-0.25 V steel. As an alternative, data-driven approaches may bring new solutions. In recent years, ML has been more and more applied on material creep performance prediction. For instance, Liu et al. [73] employed machine learning algorithms to take alloy composition, temperature, stress, heat treatment process and several microstructural parameters into

the creep life prediction of Ni-based single crystal superalloys; Zhang et al. [74] proposed a ML-based life predictor for 316L steel under creep, fatigue and creep-fatigue conditions; Zhang et al. [75] utilized physics-informed neural network (PINN) to introduce domain knowledge into ML models, which was proved to overcome the conundrum of small creep dataset; Lu et al. [76] developed multi-fidelity neural network (MFNN) based on transfer learning [77] and residual network [78], which offers new avenues for creep behavior prediction. As can be found, ML methods can learn the underlying mechanisms from high-quality small datasets and model complicated correlations among various factors with little consideration of their physical backgrounds [79].

Based on the above analysis, ML is thought to be capable of predicting long-term creep life of deformed 2.25Cr-1Mo-0.25 V steel from short-term creep rupture data. According to the general workflow of ML [80], the warm deformation process, relevant microstructural damages, heat treatment parameters, creep temperature and creep stress can be considered into the creep life prediction model of 2.25Cr-1Mo-0.25 V steel. The key to success resides in building a high-quality experimental dataset for model training. Thus, acceleration creep tests of 2.25Cr-1Mo-0.25 V steel with different deformation extents should be performed at different temperatures and stress levels. The application of physics-informed constraint and transfer learning could reduce the amount of data required. Notably, we did not include the specific implementation process of ML in this work, but provide some ideas for reference only. Thus, the above arguments have not been evidenced here and should be explained with caution.

Conclusions

In this work, the impact of warm bending on the microstructure and creep behavior of 2.25Cr-1Mo-0.25 V steel plate was investigated by SEM, EDS, EBSD, 3D μ -XCT and creep rupture tests. Notably, the creep tests were only performed under 482 °C and constant load corresponding to initial stress levels of 350 MPa. Following conclusions can be drawn.

- (1) Warm bending leads to a significant degradation of creep performance of 2.25Cr-1Mo-0.25 V

steel plate, and the surface regions are more severely deteriorated than the central region, resulting in an uneven distribution of creep property along the thickness direction of ring shell. This inhomogeneity persists after $705\text{ }^{\circ}\text{C} \times 8\text{ h}$ tempering, which may serve as a potential risk for long-term operation of 2.25Cr-1Mo-0.25 V steel ring shell.

- (2) Warm bending triggers the degradation of multiple microstructures, which unfortunately persists after $705\text{ }^{\circ}\text{C} \times 8\text{ h}$ tempering. Owing to the energy input of ring shell fabrication, carbides are coarsened, segregated and clustered, impairing the ability to hinder dislocation motion as well as providing numerous sites for cavity initiation. Moreover, the plastic strain generated by warm bending causes some of bainite grains rotate to softer orientations and highly promotes the formation of microvoid defects at the same time.
- (3) After warm bending and subsequent tempering, the plasticity resistance of 2.25Cr-1Mo-0.25 V steel is significantly reduced due to the deterioration of multiple microstructures, resulting in a faster creep strain rate controlled by the dislocation creep mechanism as well as an easier cavity nucleation caused by the debonding of the interface between larger carbides and softer matrix. Additionally, the higher void number density and void volume fraction induced by warm bending can also accelerate the ductile damage progression of 2.25Cr-1Mo-0.25 V steel under creep exposure load.

Acknowledgements

This research is supported by National Natural Science Foundation of China (Grand No. 51905173). We sincerely thank Shanghai Yinghua Testing Co., Ltd. for providing the device of GE Phoenix Nanotom M and the commercial software of VG Studio MAX 3.4. We acknowledge Jie Tang for his help during the μ -XCT tests.

Author contribution

YL contributed to investigation, experiment, data analysis, software, visualization, writing—original draft and writing—review and editing; SH contributed to conceptualization, supervision, founding acquisition and project administration; HH contributed to conceptualization and supervision; YH contributed to data analysis and investigation; JH contributed to data analysis and visualization; ZC contributed to founding acquisition and project administration.

Declarations

Conflicts of interest We declare that we do not have any commercial or associative interest that represents a conflict of interest in connection with the work submitted.

Supplementary Information: The online version contains supplementary material available at <https://doi.org/10.1007/s10853-023-08259-z>.

References

- [1] Zhou Y, Xuedong C, Zhichao F, Peng X, Xiaoliang L (2018) Effect of hydrogen on creep behavior of a vanadium-modified CrMo steel and its continuum damage analysis. In: Proceedings of the ASME 2018 Pressure Vessels and Piping Conference: PVP2018–84291, V06AT06A050 <https://doi.org/10.1115/PVP2018-84291>
- [2] Xin S, Zelin H, Bin L, Mu Q, Yuancai D, Yan S, Guangxu C (2019) Investigation of hydrogen diffusion characteristics of the heat affected zone of 2.25Cr-1Mo-0.25V steel by an electrochemical permeation method. In: Proceedings of The ASME 2019 Pressure Vessels and Piping Conference: PVP2019-93568, V001T01A076 <https://doi.org/10.1115/PVP2019-93568>
- [3] Yan S, Mengyu C, Weijie W, Yilun L, Mu Q, Guangxu C (2018) Experimental investigation of the effect of hydrogen on fracture toughness of 2.25Cr-1Mo-0.25V steel and welds after annealing. *Materials* 11(4):499. <https://doi.org/10.3390/ma11040499>
- [4] Xuedong C, Zhichao F, Jie D, Mingdong H, Shantung T, Cengdian L (2021) Technical progress review and prospect of safety guarantee for long-term service hydrogenation reactors. In: Proceedings of the ASME 2021 Pressure Vessel and Piping Conference: PVP2021-64839, V001T01A054 <https://doi.org/10.1115/PVP2021-64839>

- [5] Yafei W, Songyan H, Yun L, Guangxu C (2019) Improved hydrogen embrittlement resistance after quenching-tempering treatment for a Cr–Mo–V high strength steel. *Int J Hydrogen Energy* 44(54):29017–29026. <https://doi.org/10.1016/j.ijhydene.2019.09.142>
- [6] Cathleen S, Leslie A, Kuntak D (2019) Industry experience fabricating hydroprocessing reactors using 225Cr-1Mo-V steel. *Proceedings of the ASME 2019 Pressure Vessel and Piping Conference: PVP2019-93229, V06BT06A002* <http://doi.org/10.1115/PVP2019-93229>
- [7] Liping W, Yu L (2021) Design methods for hydrogenation reactors of 2.25Cr-1Mo-V considering creep. *Press Vessel Technol* 38(12):62–69
- [8] Yan S, Mengyu C, Junnan L, Zelin H, Pan L, Haoqi Y, Zhendong S (2022) Creep rupture behavior of 2.25Cr1Mo0.25V steel and weld for hydrogenation reactors under different stress levels. *Rev Adv Mater Sci* 61:334–349. <https://doi.org/10.1515/rams-2022-0037>
- [9] Yan S, Mengyu C, Zelin H, Pan L (2022) High-temperature tensile and creep behavior in a CrMoV steel and weld metal. *Materials* 15(1):109. <https://doi.org/10.3390/ma15010109>
- [10] Liang C, Xuedong C, Zhichao F, Yu Z, Zhenxing W, Qingfeng C (2021) Characterization of heterogeneous creep deformation in vanadium-modified 2.25Cr-1Mo steel weldments by digital image correlation. *Mater Sci Eng A* 816:141350. <https://doi.org/10.1016/j.msea.2021.141350>
- [11] Hannah S, Christian F-R, Ronny K, Martin S-N, Ronald S (2021) On the impact of post weld heat treatment on the microstructure and mechanical properties of creep resistant 2.25Cr-1Mo-0.25V weld metal. *J Mater Sci* 56:20208–20223. <https://doi.org/10.1007/s10853-021-06618-2>
- [12] Bin Y, Fuzhen X, Xiping L (2017) Heterogeneous creep behavior of a CrMoV multi-pass weld metal. *Mater Sci Eng A* 690:6–15. <https://doi.org/10.1016/j.msea.2017.02.084>
- [13] You L, Zhiping C, Pen J, Delin Z, Dong X, He M, Song H (2020) Influence of thick plate bending process on material strength distribution in hydrogenation reactor shells. *J Mater Eng Perform* 29(10):5158–5173. <https://doi.org/10.1007/s11665-020-05020-4>
- [14] Song H, Zhiping C, You L, Delin Z (2019) Impact of hot bending forming on the high temperature mechanical properties and hydrogen damage of 2.25Cr-1Mo-0.25V steel. *J Mater Eng Perform* 28(1):567–577. <https://doi.org/10.1007/s11665-018-3777-9>
- [15] Yafei W, Guangxu C, Mu Q, Qing L, Zaixiao Z, Kang C, Yun L, Haijun H, Wei W, Jianxiao Z (2017) Effect of high temperature deformation on the microstructure, mechanical properties and hydrogen embrittlement of 2.25Cr-1Mo-0.25 V steel. *Int J Hydrogen Energy* 42(38):24549–24559. <http://doi.org/10.1016/j.ijhydene.2017.07.2375>
- [16] Wei Z, Xiaowei W, Haofeng C, Tianyu Z, Jianming G (2019) Evaluation of the effect of various prior creep-fatigue interaction damages on subsequent tensile and creep properties of 9%Cr steel. *Int J Fatigue* 125:440–453. <https://doi.org/10.1016/j.ijfatigue.2019.04.018>
- [17] Petr K, Jiří D, Wolfgang B, Václav S, Zenji H, Yoichi T, Yongpeng T, Lenka K, Radim K, Marie K, Marie S (2020) The effect of predeformation on creep strength of 9% Cr steel. *Materials* 13(23):5330. <https://doi.org/10.3390/ma13235330>
- [18] Chaudhuri S, Ghosh RN (2009) Creep behavior of 2.25Cr1Mo steel—effects of thermal ageing and pre-strain. *Mater Sci Eng A* 13(23):5330. <https://doi.org/10.3390/ma13235330>
- [19] Hosseini E, Kalyanasundaram V, Li X, Holdsworth SR (2018) Effect of prior deformation on the subsequent creep and anelastic recovery behaviour of an advanced martensitic steel. *Mater Sci Eng, A* 717:68–77. <https://doi.org/10.1016/j.msea.2018.01.049>
- [20] Shaoshi R, Qinan H, Xue W, Jiamin Z, Zhipeng C, Dong D, Huiji S (2022) Long-term service induced mechanical properties change of hot-end welding metals in a retired CrMoV bainitic gas turbine rotor. *Mater Sci Eng A* 833:142323 <https://doi.org/10.1016/j.msea.2021.142323>
- [21] Hui K, Junjie S, Hongguang H, Shanjun Z, Fuyong H, Biao H, Qingquan Z, Gongye X (2020) Influence of long-term thermal ageing (> 10,000h) on low stress creep deformation of P92 heat-resistant steels. *Mater High Temp* 37(3):196–206. <https://doi.org/10.1080/09603409.2020.1740488>
- [22] Dingyi S, Hyungsoo L, Changwoo J, Allan B, Sharvan K, Ihho P, Yunjo R, Raghavan A (2019) Evolution of microstructure and creep behavior in an Fe–Ni–Cr–Nb–C alloy during service in hydrocarbon cracker tubes. *J Mater Eng Perform* 28:6588–6602. <https://doi.org/10.1007/s11665-019-04447-8>
- [23] Huitao C, Wei L, Wei C, Jian C, Shengde Z (2022) Influence of prior creep-fatigue exposure on remnant tensile and creep properties of AISI 321 austenite stainless steel. *Int J Fatigue* 159:106826 <https://doi.org/10.1016/j.ijfatigue.2022.106826>
- [24] Shaoshi R, Yibo S, Yanan F, Qinan H, Lisha N, Huiji S, Keita H, Nobuyoshi K (2018) EBSD analysis of creep deformation induced grain lattice distortion: a new method for creep damage evaluation of austenitic stainless steels. *Mater Sci Eng A* 733:329–337. <https://doi.org/10.1016/j.msea.2018.07.058>
- [25] Runzi W, Lvyi C, Shunpeng Z, Pengcheng Z, Hideo M, Xiancheng Z, Shantung T (2021) Semi-quantitative creep-

- fatigue damage analysis based on diffraction-based misorientation mapping and the correlation to macroscopic damage evolutions. *Int J Fatigue* 149:106227 <https://doi.org/10.1016/j.ijfatigue.2021.106227>
- [26] Yi G, Timothy LB, Samuel AM, Michael D, Andrew HS, Philip JW (2022) 4D imaging of void nucleation, growth, and coalescence from large and small inclusions in steel under tensile deformation. *J Mater Sci Technol* 123:168–176. <https://doi.org/10.1016/j.jmst.2022.01.024>
- [27] Yafei W, Hiroyuki T, Yuantao X, Kazuyuki S, Kyosuke H, Hiro F, Akihisa T, Masayuki U (2022) In-situ 3D observation of hydrogen-assisted particle damage behavior in 7075 Al alloy by synchrotron X-ray tomography. *Acta Mater* 227:117658 <https://doi.org/10.1016/j.actamat.2022.117658>
- [28] Xiaoqing S, Haiming Z, Zhenshan C, Fu MW, Jianbo S (2020) A multiscale investigation into the effect of grain size on void evolution and ductile fracture: experiments and crystal plasticity modeling. *Int J Plast* 125:133–149. <https://doi.org/10.1016/j.iplas.2019.09.009>
- [29] Lin YC, Xianyang W, Xiaomin C, Jian C, Dongxu W, Jinlong Z, Leiting L (2015) EBSD study of a hot deformed nickel-based superalloy. *J Alloys Compd* 640:101–113. <https://doi.org/10.1016/j.jallcom.2015.04.008>
- [30] Kai Z, Xinbao L, Lin Z (2021) Characterisation of microstructure evolution during creep of P91 steel using the electron backscatter diffraction technique. *Mater High Temp* 38(3):158–165. <https://doi.org/10.1080/09603409.2021.1897941>
- [31] Saeidi N, Ashrafizadeh F, Niroumand B, Barlat F (2015) EBSD study of damage mechanisms in a high-strength ferrite-martensite dual-phase steel. *J Mater Eng Perform* 24:53–58. <https://doi.org/10.1007/s11665-014-1257-4>
- [32] Michael D (2014) Advanced imaging and mechanistic modelling of ductile fracture. In: PhD Dissertation, University of Manchester
- [33] Fang H, Versteyleen CD, Zhang S, Yang Y, Cloetens P, Ngantillard D, Brück E, van der Zwaag S, van Dijk NH (2016) Autonomous filling of creep cavities in Fe–Au alloys studied by synchrotron X-ray nano-tomography. *Acta Mater* 121:352–364. <https://doi.org/10.1016/j.actamat.2016.09.023>
- [34] Isaac A, Sket F, Reimers W, Camin B, Sauthoff G, Pyzalla AR (2008) In situ 3D quantification of the evolution of creep cavity size, shape, and spatial orientation using synchrotron X-ray tomography. *Mater Sci Eng A* 478(1–2):108–118. <https://doi.org/10.1016/j.msea.2007.05.108>
- [35] Liyi W, Zhuman S, Xuemei L, Guangping Z (2018) 3D X-ray tomography characterization of creep cavities in small-punch tested 316 stainless steels. *Mater Sci Eng A* 724:69–74. <https://doi.org/10.1016/j.msea.2018.03.048>
- [36] “Metallic materials - Uniaxial creep testing method in tension” GB/T 2039–2012, Chinese Standard, 2012
- [37] “Steels for Hydrogen Service at Elevated Temperatures and Pressures in Petroleum Refineries and Petrochemical Plants” API Recommended Practice 941, 2016
- [38] “Boiler and Pressure Vessel Code Section VIII - Rules for Construction of Pressure Vessels Division 2 - Alternate Rules” ASME, 2021
- [39] “Fabrication Considerations for Vanadium-Modified Cr-Mo Steel Heavy Wall Pressure Vessels” API Technical Report 934-B, 2022
- [40] Zhengkai W, Shengchuan W, Jianguang B, Weijian Q, Suleyman K, Wei S, Philip JW (2021) The effect of defect population on the anisotropic fatigue resistance of AlSi10Mg alloy fabricated by laser powder bed fusion. *Int J Fatigue* 151:106317 <https://doi.org/10.1016/j.ijfatigue.2021.106317>
- [41] Philip JW, Charles B, Simone C, Veerle C, David G, Charlotte KH, Eric M, Marena M, Anton DP, Stuart RS (2021) X-ray computed tomography. *Nature Rev Methods Primers* 1:18. <https://doi.org/10.1038/s43586-021-00015-4>
- [42] YN Hu, SC Wu, PJ Withers, J Zhang, HYX Bao, YN Fu, GZ Kang (2020) The effect of manufacturing defects on the fatigue life of selective laser melted Ti–6Al–4V structures. *Mater Des* 192:108708 <https://doi.org/10.1016/j.matdes.2020.108708>
- [43] Yu P, Guorong Z, Yuxuan Q, Qiang Z (2020) In-situ assessment of the water-penetration resistance of polymer modified cement mortars by μ -XCT, SEM and EDS. *Cement Concr Compos* 114:103821 <https://doi.org/10.1016/j.cemconcomp.2020.103821>
- [44] Siefert JA, Parker JD (2016) Evaluation of the creep cavitation behavior in grade 91 steels. *Int J Press Vessels Pip* 138:31–44. <https://doi.org/10.1016/j.ijpvp.2016.02.018>
- [45] Dan W, Fuming W, Jin C, Changrong L (2018) Effects of Nb and tempering time on carbide precipitation behavior and mechanical properties of Cr–Mo–V steel for brake discs. *Steel Res Int* 89:1700491. <https://doi.org/10.1002/srin.201700491>
- [46] Hannah S, Thomas K, Manfred B, Ronny K, Hannes P, Martin P, Ronald S (2022) High-resolution characterization of precipitates in multi-layer submerged-arc welded 2.25Cr–1Mo–0.25V steel. *Mater Today Commun* 31:103299. <https://doi.org/10.1016/j.mtcomm.2022.103299>
- [47] Takeda H (2010) Evolution and coarsening of carbides in 2.25Cr–1Mo steel weld metal during high temperature tempering. *J Iron Steel Res Int* 17(05):74–78. [https://doi.org/10.1016/S1006-706X\(10\)60103-3](https://doi.org/10.1016/S1006-706X(10)60103-3)
- [48] Yongtao Z, Ledo M, Xiaojun W, Hanqian Z, Jinfu L (2009) Evolution behavior of carbides in 2.25Cr–1Mo–0.25V steel.

- Mater Trans 50(11):2507–2511. <https://doi.org/10.2320/matertrans.M2009172>
- [49] Fu RD, Yang YQ, Wang CY, Zhang WH (2008) Effects of weld thermal cycles and post-welding tempering on second phase particles in 2.25Cr-1Mo-0.25V steels. *Sci Technol Weld Joining* 13(4):349–356. <https://doi.org/10.1179/174329308X283848>
- [50] Cunyu W (2006) Study on hot deformation behavior and strain induced precipitation in 2.25Cr-1Mo-0.25V steel. In: Master Dissertation, Yansan University
- [51] Fu RD, Wang TS, Zhou WH, Zhang WH, Zhang FC (2007) Characterization of precipitates in a 2.25Cr-1Mo-0.25V steel for large-scale cast-forged products. *Mater Charact* 58(10):968–973. <https://doi.org/10.1016/j.matchar.2006.10.002>
- [52] Zhonghua J, Pei W, Dianzhong L, Yiyi L (2015) Effects of tempering temperature on the microstructure and mechanical properties of granular bainite in 2.25Cr-1Mo-0.25V steel. *Acta Metall Sin* 51(8):925–934. <https://doi.org/10.1016/j.msea.2015.03.102>
- [53] Caillard D, Martin JL (2003) Experimental studies of Peierls–Nabarro-type friction forces in metals and alloys. Pergamon Materials Series, Pergamon, pp 159–224
- [54] Raj A, Roy N, Roy BN, Ray AK (2015) Life estimation and creep damage quantification of service exposed reformer tube. *High Temp Mater Processes (London)* 34(7):731–742. <https://doi.org/10.1515/htmp-2014-0111>
- [55] Goods SH, Brown LM (1979) Overview No.1—the nucleation of cavities by plastic deformation. *Acta Metall* 27(1):1–15. [https://doi.org/10.1016/0001-6160\(79\)90051-8](https://doi.org/10.1016/0001-6160(79)90051-8)
- [56] Azmi AW, Milo VK (2005) 3D analysis of creep voids in hydrogen reformer tubes. *Mater Sci Eng A* 412:222–229. <https://doi.org/10.1016/j.msea.2005.08.223>
- [57] Yuanhang W, Shangfei Q, Fenggui L, Wen L (2016) Failure transition mechanism in creep rupture of modified casting 9Cr-1.5Mo-1Co welded joint. *Mater Des* 97:268–278. <https://doi.org/10.1016/j.matdes.2016.02.107>
- [58] Thomason PF (1990) Ductile fracture of metals. Pergamon Press, Oxford, pp 30–55
- [59] Avramovic Cingara G, Saleh AR, Jain MK, Wilkinson DS (2009) Void nucleation and growth in dual-phase steel 600 during uniaxial tensile testing. *Metall and Mater Trans A* 40:3117. <https://doi.org/10.1007/s11661-009-0030-z>
- [60] Argon AS, Im J, Safoglu R (1975) Cavity formation from inclusions in ductile fracture. *Metall Trans A* 6:825. <https://doi.org/10.1007/BF02672306>
- [61] Arsenault RJ, Cadman TW (1978) Thermally-activated motion of a group of dislocations. *Scr Metall* 12(7):633–637. [https://doi.org/10.1016/0036-9748\(78\)90276-4](https://doi.org/10.1016/0036-9748(78)90276-4)
- [62] Liu J, Liu W, Hao Z, Shi T, Kang L, Cui Z, Di Y (2020) Effects of silicon content and tempering temperature on the microstructural evolution and mechanical properties of HT-9 steels. *Materials* 13(4):972. <https://doi.org/10.3390/ma13040972>
- [63] Bin Y, Fuzhen X (2019) Nonhomogeneous microstructure related creep damage of the CrMoV multi-pass weld metal. *Mater Sci Eng A* 763:138122. <https://doi.org/10.1016/j.msea.2019.138122>
- [64] Chao F, Zhenshan C, Xiaoqing S, Mingxiang L (2017) An evolution model for elliptic-cylindrical void in viscous materials considering the evolvments of void shape and orientation. *Mech Mater* 112:101–113. <https://doi.org/10.1016/j.mechmat.2017.06.002>
- [65] Lei Z, Hongyang J, Lianyong X, Yongdian H, Junjie X (2012) Experimental study on creep damage evolution process of Type IV cracking in 9Cr-0.5Mo-1.8W-VNb steel welded joint. *Eng Fail Anal* 19:22–31. <https://doi.org/10.1016/j.engfailanal.2011.09.003>
- [66] Jiaqi W, Yongzhe F, Yuan T, Xinghua Y (2021) A machine-learning approach to predict creep properties of Cr–Mo steel with time–temperature parameters. *J Market Res* 13:635–650. <https://doi.org/10.1016/j.jmrt.2021.04.079>
- [67] Yang RC, Chen K, Feng HX, Wang H (2004) Determination and application of Larson–Miller parameter for heat resistant steel 12Cr1MoV and 15CrMo. *Acta Metall Sin (English Letters)* 17(4):471–476
- [68] Pink E (1994) Physical significance and reliability of Larson–Miller and Manson–Haferd parameters. *Mater Sci Technol* 10(4):340–346. <https://doi.org/10.1179/mst.1994.10.4.340>
- [69] Bueno LO, Sordi VL (2008) Creep behavior of Fe–Mn–Al steel from 500 °C to 800 °C: part 2: aspects of rupture strength and parametric analysis. *Mater Sci Eng A* 483–484:560–563. <https://doi.org/10.1016/j.msea.2006.12.182>
- [70] Murakami S (1983) Notion of continuum damage mechanics and its application to anisotropic creep damage theory. *J Eng Mater Technol* 105(2):99–105. <https://doi.org/10.1115/1.3225633>
- [71] Evans RW, Parker JD, Wilshire B (1992) The θ projection concept—a model-based approach to design and life extension of engineering plant. *Int J Press Vessels Pip* 50(1–3):147–160. [https://doi.org/10.1016/0308-0161\(92\)90035-E](https://doi.org/10.1016/0308-0161(92)90035-E)
- [72] Jongtaek Y, Jongyup K, Youngsang N, Nho K (2003) Park Creep strain and creep-life prediction for alloy 718 using the omega method. *Met Mater Int* 9(6):555–560
- [73] Yue L, Junming W, Zhichao W, Xiao-Gang L, Maxim A, Siqi S, Chongyu W, Tao Y (2020) Predicting creep rupture

- life of Ni-based single crystal superalloys using divide-and-conquer approach based machine learning. *Acta Mater* 195:454–467. <https://doi.org/10.1016/j.actamat.2020.05.001>
- [74] Xiaocheng Z, Jianguo G, Fuzhen X (2021) A deep learning based life prediction method for components under creep, fatigue and creep-fatigue conditions. *Int J Fatigue* 148:106236 <https://doi.org/10.1016/j.ijfatigue.2021.106236>
- [75] Xiaocheng Z, Jianguo G, Fuzhen X (2021) A physics-informed neural network for creep-fatigue life prediction of components at elevated temperatures. *Eng Fract Mech* 258:108130 <https://doi.org/10.1016/j.engfractmech.2021.108130>
- [76] Lu L, Ming D, Punit K, Upadrasta R, George EK, Subra S (2020) Extraction of mechanical properties of materials through deep learning from instrumented indentation. *PNAS* 117(13):7052–7062. <https://doi.org/10.1073/pnas.1922210117>
- [77] Ivan O, Oghenejokpeme IO, Tirharaj D, Andy MD, Larisa NS, Joaquin V, Ross DK (2021) Transformational machine learning: learning how to learn from many related scientific problems. *PNAS* 118(49):e2108013118 <https://doi.org/10.1073/pnas.2108013111>
- [78] Kaiming H, Xiangyu Z, Shaoqing R, Jian S (2016) Deep residual learning for image recognition. *IEEE Conf Comput Vis Pattern Recog* 2016:770–778. <https://doi.org/10.1109/CVPR.2016.90>
- [79] You L, Zhiping C, Hongfei L, Mengjie L, Hao M, Song H (2022) Effect of tempering on bending-induced material strength inhomogeneity in hydrogenation reactor shells. *Int J Press Vessel Piping* 195:104575 <https://doi.org/10.1016/j.ijpvp.2021.104575>
- [80] Zhang A, Lipton ZC, Li M, Smola AJ. (2016) Dive into deep learning, arXiv preprint.

Publisher's Note Springer Nature remains neutral with regard to jurisdictional claims in published maps and institutional affiliations.

Springer Nature or its licensor (e.g. a society or other partner) holds exclusive rights to this article under a publishing agreement with the author(s) or other rightsholder(s); author self-archiving of the accepted manuscript version of this article is solely governed by the terms of such publishing agreement and applicable law.